NASA TECHNICAL NOTE
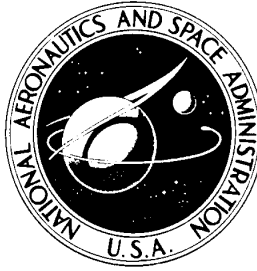
DYNAMIC ANALYSIS OF XB-70-1 INLET PRESSURE FLUCTUATIONS DURING TAKEOFF AND PRIOR TO A COMPRESSOR STALL AT MACH 2.5

by Richard A. Martin

Flight Research Center
Edwards, Calif. 93523

1. Report No. NASA TN D-5826	2. Government Accession No.	3. Recipient's Catalog No.
4. Title and Subtitle DYNAMIC ANALYSIS OF XB-70-1 INLET PRESSURE FLUCTUATIONS DURING TAKEOFF AND PRIOR TO A COMPRESSOR STALL AT MACH 2.5		5. Report Date June 1970
		6. Performing Organization Code
7. Author(s) Richard A. Martin		8. Performing Organization Report No. H-595
9. Performing Organization Name and Address NASA Flight Research Center P. O. Box 273 Edwards, California 93523		10. Work Unit No. 720-51-00-05-24
		11. Contract or Grant No.
12. Sponsoring Agency Name and Address National Aeronautics and Space Administration Washington, D. C. 20546		13. Type of Report and Period Covered Technical Note
		14. Sponsoring Agency Code

15. Supplementary Notes

16. Abstract

Instrumentation in the left inlet of the XB-70-1 airplane was used to record high-response total- and static-pressure data from 0 to 200 hertz during takeoff and immediately prior to a compressor stall at Mach 2.5 and an altitude of 63,100 feet (19,200 meters). Since the statistical assumptions of stationarity, randomness, and normality were found to be approximately valid for the inlet pressure data, random data-analysis techniques were applied. Values of mean turbulence parameter as high as 12 percent were obtained during takeoff and from 14 percent to as high as 31 percent prior to stall. The flight inlet turbulence-producing mechanism, namely, normal-shock boundary-layer interaction, can be simulated successfully in ground test facilities up to at least 40 hertz as evident in the pressure-wave power spectra; however, higher turbulence values were experienced in flight than in model tests by an engine compressor prior to stall.

17. Key Words Suggested by Author(s) Inlet—engine compatibility - Dynamic distortion - XB-70-1 airplane	18. Distribution Statement Unclassified - Unlimited		
19. Security Classif. (of this report) Unclassified	20. Security Classif. (of this page) Unclassified	21. No. of Pages 56	22. Price* $3.00

DYNAMIC ANALYSIS OF XB-70-1 INLET PRESSURE FLUCTUATIONS DURING

TAKEOFF AND PRIOR TO A COMPRESSOR STALL AT MACH 2.5

By Richard A. Martin
Flight Research Center

INTRODUCTION

The capability of predicting the combined performance of an inlet and engine under distorted flow conditions has increased in recent years through the development of various steady-flow distortion parameters based on total-pressure measurements at the inlet—engine interface plane. In addition, the necessity of understanding unsteady phenomena occurring in the air inlets of high-speed aircraft has arisen. These unsteady interactions can lead to severely reduced aircraft performance because of abrupt compressor stalls and violent inlet unstarts and, as such, pose a major problem for both civilian and military aircraft inlet and engine designers. Accordingly, considerable emphasis is being placed on inlet dynamics by government and private industry.

Turbulence-induced compressor stalls may have been first recognized in wind-tunnel engine—inlet compatibility studies of a one-third-flow-scale XB-70 inlet modified to fair into a single J93 engine (ref. 1). More than 20 stalls at Mach numbers of 2.24 to 3.00 were induced by operating the inlet at highly supercritical conditions, that is, with the normal shock relatively far downstream of the inlet aerodynamic throat.

Turbulence and dynamic distortion parameters may be defined by dynamic-pressure measurements. Values of a turbulence parameter are local measurements of normalized fluctuating pressure amplitude which, of course, may vary depending on the location and the local flow conditions. Values of a dynamic distortion parameter, however, are the calculated values of instantaneous distortion, implying a multiplicity of high-response pressure measurements. This report deals only with turbulence aspects of the dynamic measurements. Because of the random nature of the transient pressure signals, statistical methods can be applied in their analysis.

To provide inlet dynamics data from full-scale aircraft under actual flight conditions, the NASA Flight Research Center conducted flight studies with the XB-70-1 airplane. The airplane was instrumented with high-response static- and total-pressure sensors to detect the pressure fluctuations caused by any type of flow-disturbing phenomena, but particularly shock-induced boundary-layer separation and flow-turning separation. To minimize tubing transmission problems inherent in measuring dynamic pressures at remote locations, close-coupled probes and sensors were used in the left-hand inlet of the XB-70-1 airplane. The primary purpose of this study was to describe the dynamic flow conditions at various locations in a full-scale aircraft inlet by using a turbulence parameter and random data-analysis techniques and thus more

completely define the interface between inlet and engine. More advanced studies are also underway utilizing instrumentation in the inlet of an F-111A aircraft.

The data analyzed in this report were recorded onboard on one XB-70-1 flight during and slightly after takeoff and during an inlet turbulence test at Mach 2.5 immediately prior to a compressor stall. This turbulence test utilized position control of the normal shock in a started inlet through manual bypass airflow adjustments. Results from measurements of true root mean square, amplitude probability density, and power spectral density of the pressure fluctuations are presented and compared with related wind-tunnel results from references 1 and 2.

SYMBOLS

The units for the physical quantities used in this report are given in U. S. Customary Units and parenthetically in the International System of Units (SI). Factors relating the two systems are presented in reference 3.

a_l longitudinal acceleration, g

a_n normal acceleration, g

B effective filter bandwidth, Hz

D distortion parameter, $\left(p_{t_{2_{max}}} - p_{t_{2_{min}}}\right)\Big/ p_{t_{2_{av}}}$

f frequency, Hz

$G(f)$ power spectral-density function, $\lim_{B \to 0} \dfrac{1}{BT} \displaystyle\int_0^T p(f,\ t,\ B)\ dt$, $(\text{lb/in.}^2)^2\big/\text{Hz}$ $((\text{kN/m}^2)^2/\text{Hz})$

g acceleration due to gravity, ft/sec^2 (m/sec^2)

h altitude, ft (m)

L characteristic length, ft (m)

M Mach number

2

N   engine speed, rpm

n   effective number of statistical degrees of freedom for power-spectral-density estimates, $2B\tau$

p   pressure, $lb/in.^2$ (kN/m^2)

Δp peak-to-peak pressure envelope, includes 99.7 percent of the pressure excursions from the mean for a stationary signal, $lb/in.^2$ (kN/m^2)

N_{Re} Reynolds number based on duct vertical dimension of 5.375 ft (1.638 m), $\rho VL/\mu$

N_{Re_I} Reynolds number index, $\dfrac{\delta_2}{\psi_2 \Theta_2} = \dfrac{\delta_2 \left(T_{t_2} + 199.5\right)}{718.2\Theta_2^{2}}$

T   temperature, °F (°C)

Tu   turbulence parameter

t   time, sec

V   airspeed, knots

α angle of attack, deg

β angle of sideslip, deg

δ ratio of absolute total pressure to absolute pressure of ARDC model atmosphere at sea level

ϵ normalized standard error, $1/\sqrt{B\tau}$

ζ dummy variable

η total-pressure recovery, $(p_{t_2}/p_{t_\infty})_{av}$, arithmetically averaged for all probes recorded for three engines during the data-set intervals

Θ ratio of absolute total temperature to absolute temperature of ARDC model atmosphere at sea level

μ viscosity, lb-sec/ft^2 (N-sec/m^2)

ρ density, lb-sec^2/ft^4 (kg/m^3)

σ standard deviation $+\sqrt{\dfrac{1}{\tau}\displaystyle\int_0^\tau \left[p(t) - p(t)_{av}\right]^2 dt}$ (equivalent to root-mean-square value for zero mean, i.e., $p(t)_{av} = 0$)

τ effective averaging time, sec

φ angle of roll, deg

ψ ratio of absolute viscosity to absolute viscosity of ARDC model atmosphere at sea level

Subscripts:

av   average

i   integer variable 1, 2, 3. . .

max   maximum

min   minimum

rms   root-mean-square value

t   stagnation or reservoir conditions

4

∞ free-stream station

2   diffuser-exit (compressor-face) station

Δ peak-to-peak value

APPARATUS

Airplane

The delta-wing XB-70-1 airplane (fig. 1) was designed to cruise at Mach 3.0 at about 70,000 feet (21,300 meters) altitude. It had a takeoff gross weight in excess of 500,000 pounds (226,800 kilograms). Physical characteristics of the airplane are tabulated in reference 4.

Propulsion System

The propulsion system of the XB-70-1 airplane was comprised of a single nacelle integrated into the fuselage and wing and divided into twin, symmetric air-intake ducts approximately 70 feet (21.34 meters) in length. Each of the inlets provided airflow to three YJ93-GE-3 afterburning turbojet engines individually rated in the 30,000-pound (133,400-newton) sea-level static-thrust class.

A schematic drawing of the left-hand inlet is presented in figure 2. This two-dimensional, mixed-compression inlet used movable ramps to attain optimum throat areas, large bypass doors on the top of the duct forward and between the leading edge of the vertical stabilizers to match engine airflow needs, and an extensive boundary-layer bleed system in the throat region to assure shock stability in the high supersonic mode of operation.

Figure 3 is a series of schematic drawings of the left-hand inlet depicting the three modes of inlet operation: subsonic, low supersonic (up to Mach 2), and high supersonic (above Mach 2). At subsonic speeds the inlets acted as conventional diffusers. For supersonic speeds up to Mach 2.0, they maintained a system of successive oblique shock waves which terminated with a normal shock outside the inlets (external compression mode). At Mach 2.0 the normal shock was ingested to some position downstream of the inlet throat by reducing the downstream pressure through the use of the airflow bypass doors. This shock could thereafter be maintained and positioned through throat-area and bypass-door adjustments made manually by the copilot after reading the cockpit indicators (started mode). It should be noted that "supercritical," as used in the figure, implies a high supersonic mode in which the terminal shock is abnormally far downstream of the aerodynamic throat.

A more complete description of the inlet system is provided in reference 5. Reference 6 describes the XB-70-1 inlet geometries and area requirements, and propulsion-system performance substantiation data obtained during model testing are included in reference 7.

Instrumentation

To meet the need for flight-inlet dynamics data, modifications were made to some of the initially installed XB-70-1 inlet pressure-sensing instrumentation to enable it to detect rapid pressure fluctuations. Tubing lines joining probes and transducers were shortened to within 6 inches (15.24 centimeters) at selected locations, and suitable analog recording channels were selected in the data-acquisition system. These installations were then tested for frequency response to assure the absence of adverse tubing-transmission effects up to 200 hertz, as discussed in reference 8. Thus, high-frequency-response (up to 200 hertz) pressure data were recorded by mounting transducers close to the points of measurement, or by "close-coupling." (See fig. 4.)

A schematic drawing showing both the high-response and the steady-state total-pressure-instrumentation locations at the inlet exit is presented in figure 5. As shown, the four compressor rakes on each engine were oriented at 90° intervals with respect to the rake located at 22.5° counterclockwise from vertical. Each rake contained five probes spaced at the centers of equal annular flow areas. Because of the large size of the existing pressure transducers and the requirement of close coupling, the dynamic-pressure probes on engines 2 and 3 were placed in the central hub fairing and about the perimeter of the compressor face only. The locations of the high-response static-pressure sensors used in this study were shown in figure 2.

All inlet transducers used were ±6 psi (41.37 kN/m^2) differential full-scale range referenced to a plenum static.

Data-Acquisition System

The XB-70-1 airborne data-acquisition system, described in detail in references 9 to 11, was housed in a specially designed instrumentation package and stored in the aircraft's converted weapons bay. The package was cooled and pressurized. It was independent of other systems except for required electrical power. Each data channel of the package was checked prior to each test flight.

The data-acquisition system included two sections, analog and digital. Important elements in the analog section are shown in figure 6, which was adapted from reference 9. The analog section used FM techniques (see, for example, refs. 12 and 13) to record on 1-inch-wide, 14-track magnetic tape. Twelve of the tracks each contained up to 12 channels (parameter records) in an Inter-Range Instrumentation Group (IRIG) standard frequency-multiplexed format. The remaining two tracks carried tape speed compensation and time code signals. Thus, provision was made through channel selection for the acquisition of about 144 dynamic-pressure (above 20 hertz) parameters, including analog pressure data up to 200 hertz.

Approximately 800 channels of steady-state data could be recorded by the digital section. All channels were individually signal-conditioned (except thermocouples). More information on the digital section is available in references 9 to 11.

Data-Reduction System

Analog.— Figure 7 is a photograph of some of the data-reduction electronics used in this study. The main components were an oscilloscope, true root-mean-square voltmeter, oscillator, frequency counter, sweep oscillator, tracking filters, tunable low-pass filter, tunable discriminator, X-Y plotter, wave analyzer (for detecting band-limited absolute mean of signal), loop recorder (for playback of spliced magnetic-tape loops), high-response light-beam oscillograph (for playback of direct analog and true root-mean-square signals), and continuous-reel tape recorder. A probability density analyzer owned and operated by the North American Rockwell Corporation was also used.

Digital.— The general-purpose digital computers used to read and reduce digitalized data were an IBM 360 at the Flight Research Center and an IBM 7094 at North American Rockwell Corporation.

PROCEDURE

Test Description

The data analyzed were recorded on an XB-70-1 flight during and shortly after takeoff and at Mach 2.5 and an altitude of 63,100 feet (19,200 meters). The latter data resulted from a duct turbulence test performed to evaluate the effects of inlet turbulence on the engines and on inlet performance. In this test the bypass doors were opened manually to draw the normal shock system farther downstream of the throat in successive increments. As the shock system moved rearward, its strength increased.

Statistical Assumptions

Because of the apparent random nature of the high-frequency pressure oscillations observed in the inlets, statistical methods were applied in their analysis, as discussed in reference 14. However, for these methods to have been valid, the data time histories had to exhibit three basic characteristics: stationarity, randomness, and normality. (See ref. 15.) Evidence supporting the assumption that these characteristics generally do apply is provided by the following observations: (1) The mean values and root-mean-square values obtained from the data time histories did not vary significantly, and the sample lengths (5 seconds) were long compared to the duration of the pressure fluctuations; (2) the power spectra obtained from the pressure samples were characterized by an absence of spectral peaks except for the prominent 60-hertz standard alternating-current peaks and harmonics which are attributed to ground station noise; and (3) typical amplitude probability density curves were approximately Gaussian in shape, as shown in figure 8.

Furthermore, it was assumed that the statistical properties evaluated by time averaging a single record of the process were equivalent to those obtained had ensemble averaging been used (ergodic hypothesis). The terms power spectral density, ensemble, probability density function, and Gaussian distribution are defined in reference 15.

7

Analog Data Analysis

To meet statistical precision requirements, 5-second time histories were selected for stabilized conditions. These intervals were then located to within ±0.1 second using a recorded time code, carefully cut out and spliced into magnetic-tape loops. Preliminary analysis of the 5-second loops consisted of direct and true root-mean-square playback, which included low-pass filtering to 200 hertz.

Each 5-second data record was inspected for large dc shifts and large overall changes in the basic signal composition, as well as large time variations of the root-mean-square value. If any of these properties were observed, the record was assumed to be nonstationary, and no data were analyzed for that loop.

Two equivalent turbulence parameters Tu_Δ and Tu_{rms} were derived from the playbacks as outlined in the following discussion and shown schematically in figure 9, adapted from reference 2. It is significant that this equivalence holds only if the data are stationary and Gaussian. The parameter Tu_{rms} is preferred because of the simplicity of measurement.

The first parameter Tu_Δ may be defined as $\Delta p/p_{t_{2_{av}}}$ where Δp is the peak-to-peak pressure envelope which includes 99.7 percent of the pressure excursions from the mean. The value of Δp was obtained from the direct playbacks, and $p_{t_{2_{av}}}$ was derived from low-response digital data using a computer to time-average total pressure for all probes recorded over the three left-hand engines during the 5-second sample intervals.

The second turbulence parameter Tu_{rms} may be defined as $6\Delta p_{rms}/p_{t_{2_{av}}}$ for Gaussian (or normal) data where Δp_{rms} is the true root-mean-square value obtained in practice from the faired time average of the output of a calibrated meter. Figure 9 illustrates the concept underlying this equivalence, that 99.7 percent of all instantaneous readings will lie between ±3σ for zero mean. The zero-mean condition was satisfied by using equipment designed to pass only alternating and not direct current.

The approach taken in this study was to separate the dynamic component of pressure (turbulence) from the mean value for individual pressure time histories, using analog instruments. This approach differs fundamentally from directly comparing instantaneous values of a distortion parameter.

By using a wave analyzer along with playback and demultiplexing electronics, the frequency-domain function power spectral density $G(f)$ was plotted. Power spectral densities in the 3- to 200-hertz frequency range were obtained on this alternating current device by low-pass filtering or "pre-whitening" each selected analog data record to 200 hertz, bandpass filtering with a sharp 5-hertz filter, detecting the absolute average of the band-pass filter output, log-converting, and, finally, plotting on semilogarithmic paper with a scale factor of 10 decibels per decade (effectively squaring).

A scale calibration factor (for peak preset at 0.71-root-mean-square volt or 1.00-volt amplitude for a sine wave) was applied to normalize the power-spectral-density

8

function to

$$\frac{G(f)}{\left(p_{t_{2_{av}}}\right)^2} = \frac{\left(\frac{\Delta p_{rms}}{p_{t_{2_{av}}}}\right)^2}{B}$$

in units of 1/hertz. From this function the parameter $Tu_{rms} = \frac{6\Delta p_{rms}}{p_{t_{2_{av}}}}$ may be

derived by integrating over the frequency spectrum, taking the square root, and multiplying by 6; that is,

$$Tu_{rms} = \frac{6\Delta p_{rms}}{p_{t_{2_{av}}}} = 6\left[\int_3^{200} \frac{1}{\left(p_{t_{2_{av}}}\right)^2} G(f)df\right]^{1/2}$$

where the "area under a PSD [power spectral density] curve" equals $\int_3^{200} \frac{1}{\left(p_{t_{2_{av}}}\right)^2} G(f)df$.

In this way, the total area under a power-spectral-density curve is related simply and directly to the level of turbulence.

Digital Data Analysis

A Fortran IV computer program was written to calculate the following steady-state parameters: average total pressure $p_{t_{2_{av}}}$, total-pressure recovery η, distortion D, and Reynolds number based on the vertical dimension of the inlet opening N_{Re}. Total-pressure recovery was calculated by using the expression

$$\eta = \left(\frac{p_{t_2}}{p_{t_\infty}}\right)_{av}$$

where an arithmetic average of all probes recorded for the three left-hand engines was time-averaged during the 5-second time-history intervals.

Distortion for each engine was calculated by using the equation

$$D_i = \frac{\left(p_{t_{2_{max}}} - p_{t_{2_{min}}}\right)_i}{\left(p_{t_{2_{av}}}\right)_i}$$

where the largest difference in total pressure is divided by the average total pressure for each engine i. An average distortion D was then found by arithmetically

9

averaging D_i for the three engines and time-averaging the result as in the calculation of total-pressure recovery.

These time-averaging procedures were used in the calculation of average pressure, recovery, and distortion so that 5-second estimates of average pressure could be introduced into the digital program by means of card input. In this way data for compressor-face sensors recorded by the analog system only were included.

Values of indicated Mach number used in processing the data were corrected for position error of the aircraft nose-boom static-pressure orifices.

PRECISION

In the manner of reference 12, measurement errors may be classified as either systematic or random. Systematic errors can be theoretically eliminated by calibration or some form of compensation, and random errors or noise can be reduced by such factors as good design, and averaging processes, but generally not eliminated.

Systematic Errors

The systematic errors in the XB-70-1 data-acquisition system (all inlet transducers were ±6 psi (41. 37 kN/m^2) differential full-scale range referenced to a plenum static) were no greater than 2. 5 percent of full scale for the static pressures and 1. 5 percent of full scale for the total pressures. These approximations include systematic errors up to the time of magnetic-tape playback.

As part of the calibration procedure before each playback run, the analog printing devices were recalibrated and a reproducibility check was made on the power-spectral-density plots in deference to the many variables inherent in the data playback system. (See ref. 14.) During each playback the data signals were filtered with a 200-hertz low-pass filter which was flat in frequency response to 200 hertz and had a rolloff rate of 18 decibels per octave.

As described previously, a composite calibration factor was applied to the power-spectral-density curves to obtain units of 1/hertz. Also, zero-shift corrections were made to the mean differential-pressure readings obtained from oscillograph strip-outs before the values were input to a digital computer to account for deviations of the actual center frequencies from IRIG standards.

Random Errors

The random errors present in the pressure data were a major problem and were dealt with in the following manner. The time histories are composites of turbulence, tube resonances, compressor noise, electronic noise, and, possibly, structural vibrations. An attempt was made to identify the compressor noise, electronic noise, and structural vibrations in a systematic fashion by simultaneously recording the signal obtained from a transducer on engine 2 (originally connected to rake 4, probe 2)

10

which had been "capped" by disconnecting the normal tubing and connecting the input (pressure) and reference (static) sides of the sensor with a short length of new tubing to obtain a differential null. Thus, the data for the capped transducer contained "turbulence level" contributions from all sources other than aerodynamic typical of, but not, of course, identical to those inherent in all the measurements. Although these data were not applied as a corrective factor, for example, by subtracting capped from uncapped Tu_{rms} levels, they are included in later figures as reference levels.

The smooth power spectra presented in this report are the result of hand averaging the raw power-spectral-density estimates as recommended in reference 16 to increase accuracy.

Reference 16 also states that for a given highly resolved estimate of power spectral density, the error between the measured and the true power density will be $\pm\epsilon = 1/\sqrt{B\tau}$ (where ϵ is called the "normalized standard error," B is the effective filter bandwidth, and τ is the effective averaging time) with a confidence factor of 67 percent if $\epsilon \leqq 0.2$. That is, two-thirds of the measurement will be within $\pm\epsilon$. For this study $\epsilon = 0.2$.

An additional measure of statistical accuracy is the number of statistical degrees of freedom n which is the number of independent variables in the estimate of a quantity. The effective number of degrees of freedom for spectral density estimates is given by $n = 2B\tau$. For this study, $n = 50$ since $B = 5$ hertz and $\tau = 5$ seconds.

RESULTS AND DISCUSSION

Test Results

Figures 10 and 11 are time histories of selected aircraft parameters during the two test conditions, takeoff and Mach 2.5, respectively. As shown, eight 5-second intervals at relatively stabilized conditions were selected for analysis. To facilitate reference to the eight intervals, the collection of total- and static-pressure time histories recorded for each interval are referred to as a "data set." Data sets A to D of figure 10 comprise the intervals selected during takeoff for evaluation of sharp-lip effects. Data sets E to H of figure 11 comprise the intervals selected during the inlet turbulence test to determine the nature of the pressure fluctuations for increasingly supercritical operating conditions prior to stall.

In figure 10 data set A began about 10 seconds before brake release (indicated by the initial rise in longitudinal acceleration) with the engines at military power setting. About 9 seconds after brake release with full thrust developed and a constant acceleration of about 0.25g, data set B started. About 30 seconds later, but 10 seconds prior to rotation (indicated by the rise in α), data set C started, and during the initial climbout data set D sampled 5 seconds of data.

Also shown in figure 10 are photographs of actual analog data samples for a typical compressor-face total-pressure probe (engine 2, rake 4, probe 5) and the sealed transducer. The parameters Tu_Δ and Tu_{rms} were derived from similar data for all probes used in the analysis. Pressure amplitude changed between data sets for the

11

total-pressure probe from an initial level noticeably higher than that for the capped transducer.

Data sets E to H, shown in figure 11, were selected to include stabilized conditions at Mach 2.5 and an altitude of 63,100 feet (19,200 meters) with successively higher supercritical inlet operating conditions induced by opening the bypass doors. Table I summarizes the nominal bypass-door openings and the maximum durations of stabilized flight times over which the accompanying bypass settings were held.

TABLE I.— NOMINAL BYPASS-AREA SETTINGS DURING
THE TURBULENCE TEST

	Data set			
	E	F	G	H
Bypass area, in.^{2} (cm^2)	540 (3480)	940 (6065)	1340 (8650)	1600 (10,300)
Duration, sec	12	20	42	6.5

At a bypass-door opening of 940 square inches (6065 square centimeters) the copilot observed a slight increase in airframe buffet and "duct rumble" and noted, "The next bypass setting was to 1340 sq. in., and the airframe buffet and duct rumble increased considerably." This final setting of 1600 square inches (10,300 square centimeters) was selected near a stall-margin limit on bypass area indicated by flight-test experience. However, engine 2 stalled 6.5 seconds after 1600 square inches (10,300 square centimeters) was set; at the previous setting, conditions were steady for 42 seconds with no indication of a compressor stall. Figure 11 shows that data set H was recorded immediately before the rise in turbine exhaust gas temperature for engine 2 which accompanied the compressor surge.

Analog data are shown in figure 11 for a total-pressure probe (engine 2, rake 4, probe 5) and for the capped transducer (engine 2). The amplitude of the total-pressure oscillations increased as the inlet became more supercritical.

Table II presents steady-state parameters for each data set.

TABLE II.— SUMMARY OF XB-70 STEADY-STATE FLIGHT DATA

Data set	Condition	Mach number, M_∞	Altitude h, ft (m)	Mean free-stream recovery, η, percent	Mean total-pressure distortion, D, percent	Reynolds number, N_{Re}	Reynolds number index, N_{Re_I}	Mean total pressure, $p_{t_{2_{av}}}$, lb/in.^{2} (kN/m^2)	Total temperature, T_t, °F (°C)
A	Takeoff	0	2.28×10^3 (0.695×10^3)	87.4	10.2	------	----	11.821 (81.503)	66.9 (19.4)
B		.05	2.28 (.695)	88.7	10.5	1.585×10^6	----	12.025 (82.909)	66.3 (19.1)
C		.25	2.28 (.695)	93.1	14.5	8.534	----	13.164 (90.763)	71.0 (21.7)
D		.42	3.49 (1.06)	95.8	13.4	13.685	----	13.945 (96.147)	95.1 (35.1)
E	Turbulence	2.50	63.1 (19.2)	82.3	5.7	8.608	1.20	12.705 (87.598)	402.4 (205.8)
F	test	2.49	63.1 (19.2)	74.4	6.5	8.601	1.11	11.356 (78.359)	398.5 (203.6)
G		2.50	63.1 (19.2)	68.2	10.8	8.704	1.06	10.938 (75.415)	395.9 (202.2)
H*		2.49	63.1 (19.2)	65.7	11.4	8.698	.98	10.037 (69.203)	391.3 (199.6)

*Immediately prior to stall.

Turbulence Results

An attempt was made earlier to justify the necessary assumptions of stationarity and normality. If they were, in fact, exact for the present data, the turbulence amplitude obtained by directly measuring the waveform envelope Tu_Δ would agree perfectly with the envelope calculated from the root-mean-square value Tu_{rms}. Figure 12 compares the two definitions, including all Tu_{rms} and Tu_Δ values obtained for this study, and shows a divergence from perfect agreement as the turbulence level increases; Tu_Δ is generally larger than Tu_{rms} for turbulence parameter levels above about 15 percent. This is to be expected since variations in the mean pressure over the interval of measurement (effect of nonstationarity) will contribute to an increase in the measured peak-to-peak amplitude.

Figure 13 presents flight turbulence and steady-state distortion data for the takeoff and turbulence test segments. Turbulence Tu_{rms} versus inlet recovery η is shown in figures 13(a) and 13(e) for the throat and duct static pressures. (See also fig. 2.) For the capped probe, Tu_{rms} does not exceed 4 percent during either test. Thus, 4 percent is roughly the noise reference level; that is, the "turbulence level" of non-aerodynamic sources is less than 4 percent for all conditions.

During the takeoff segment (figs. 13(a) to 13(d)), the turbulence due to sharp-lip flow separation was expected to be reduced as the aircraft velocity increased, the flow streamlines into the capture area became straight, and the recovery increased. In figure 13(a) the throat static-pressure turbulence rises initially and then decreases as expected, whereas the duct static pressure shows negligible turbulence compared with the capped-transducer level. At engine 3 compressor face (fig. 13(b)), however, the mean total-pressure turbulence, shown by a broken line, remains nearly constant at 11 percent. At engine 2 compressor face (fig. 13(c)), the mean turbulence decreases from about 12 to 7 percent.

Average steady-state distortion during the takeoff test shown in figure 13(d) increases about 4.5 percent, from near 10 percent prior to brake release to 14.5 percent just prior to lift-off (data set C). Recovery increased from approximately 87 percent to 96 percent between data sets A and D, respectively.

During the Mach 2.5, or turbulence test, segment (figs. 13(e) to 13(h)), Tu_{rms} for both static-pressure sensors (fig. 13(e)) increases at the successively lower recovery points. The variation in recovery was from about 82 percent to 66 percent between data sets E and H, respectively. As the pressure recovery decreased in this test, the mean Tu_{rms} curve for available high-response engine 3 parameters (fig. 13(f)) increased approximately 17 percent. Comparison of the mean Tu_{rms} levels for engine 2 (fig. 13(g)), which stalled immediately after data set H was recorded, with the mean Tu_{rms} curve from figure 13(f) shows that although the overall rise in mean Tu_{rms} for engine 2 (about 17 percent) with decreasing recovery matches that for engine 3, the percentage increases from data set G to H do not. In these data sets, the mean Tu_{rms} for engine 3 increases only 1 percent, whereas the mean Tu_{rms} for engine 2 increases 5 percent.

13

Average steady-state distortion D during the turbulence test shown in figure 13(h)
rises approximately 6 percent, from about 5.7 percent at data set E to 11.4 percent at
data set H. The largest change, about 4 percent, occurred between data sets F and G,
whereas the change from data set G to H prior to stall is only about 0.5 percent.

Several points are noteworthy. Although reference has been made to the nominal
bypass settings, they are of only secondary interest. The primary independent param-
eter for the turbulence test was terminal shock strength. However, recovery may be
taken as a direct measure of terminal shock strength, since total-pressure losses
upstream of the shock were essentially constant. A digital simulation of the XB-70
inlet for Mach 2.5 showed this to be a valid assumption downstream of the throat where
the variation of duct cross-sectional area was linear with distance down the duct. (See
ref. 5.) Figure 13 shows Tu_{rms} to be approximately linear with recovery.

The increase in turbulence with decreasing recovery or increasing shock strength
in figures 13(e) to 13(g) agrees with the observations made in references 1 and 2. It
is believed that the turbulence-producing mechanism was a strong shock-wave,
boundary-layer interaction in the inlet. As the normal-shock system was drawn aft of
the throat region, which was a porous boundary-layer bleed region, and into a diverging
nonporous area, the shock strength consequently increased while the boundary layer
thickened. As a result, it is believed that the separated boundary layer was mixed
with the core flow and carried downstream into the engines. Thus, the flow field at the
compressor face probably contained turbulence due to shock oscillation and separated
boundary layer.

The occurrence of the XB-70-1 engine 2 compressor stall seconds after the copilot
set 1600 square inches (10,300 square centimeters) on the bypass control (data set H,
figs. 11 and 13) and not while the control was set for 1340 square inches (8650 square
centimeters) (data set G, figs. 11 and 13), which was held stabilized for 42 seconds,
indicates that the combination of distortion and turbulence levels for data set H had
reduced the engine stall margin to zero.

Finally, there was a pronounced upward shift of Tu_{rms}, shown in figure 13(g),
between data sets G and H for engine 2 that was not evidenced by engine 3 in figure 13(f).
It may be significant that the engine 2 compressor stall followed this local rise in
Tu_{rms}.

Power-Spectral-Density Analysis

When random data-analysis techniques are used, time, frequency, and amplitude-
dependent properties of the data of interest can be isolated. The power-spectral-
density function G(f) establishes the data frequency composition, which in this study
is of interest from probe to probe for differing inlet operating conditions.

Normalized pressure power-spectral-density curves are presented for the takeoff
and Mach 2.5 turbulence-test segments in figures 14 and 15, respectively. The four
curves in each plot of figure 14 represent power-spectral-density estimates for an
individual probe during data sets A to D, respectively. Similarly, in figure 15 the
curves are members of the data sets denoted by E, F, G, or H. In both figures data
are presented, in sequence, for the capped transducer (engine 2), the two static-pressure

14

sensors, two total-pressure probes from engine 3, and four total-pressure probes from engine 2.

The capped-transducer spectral distribution provided in figure 14(a) as a noise reference level shows a rapid decrease in energy up to 40 hertz from power levels between 1.6×10^{-6} and 5.4×10^{-6} at 3 hertz. Above 40 hertz the curves maintain a level below 10^{-7}. These trends are interrupted by four severe, sharp peaks at 30, 60, 90, and 120 hertz. The peaks are believed to be characteristic of 60-hertz ground station noise pickup and harmonics and may thus be discounted where they appear regularly in subsequent figures at low-to-moderate power levels.

Figure 14(b) presents data for the throat static-pressure sensor located approximately 10.5 feet (3.20 meters) downstream of the nacelle lip. The change in overall area under the curves agrees with the corresponding data points in figure 13(a). This was expected, inasmuch as the area under each curve is simply related to Tu_{rms}.

Figure 14(c) shows that the duct static-pressure sensor detected little of the power exhibited by the throat static-pressure sensor for the takeoff segment; in fact, a comparison with figure 14(a) (capped transducer) shows that the duct sensor exhibited little energy above the noise level, again in agreement with figure 13(a). Therefore, the throat static-pressure sensor may have been measuring static-pressure fluctuations resulting from highly turbulent flow separation over the sharp lip during takeoff. However, the large size and geometry of the diffuser apparently attenuated the local static-pressure oscillations by the time the airflow reached the compressors.

The shapes of the total-pressure power spectra for probes on engine 3, shown in figures 14(d) and 14(e), are noticeably different from those of the static-pressure power spectra. This might be expected, since the total-pressure probes detect impact-pressure fluctuations. The spectra reveal a decrease in energy with frequency which is most rapid between 3 hertz and 40 hertz and then more gradual up to 200 hertz. The overall level change is about one order of magnitude (10 dB). In these figures the 60-hertz noise peaks are less prominent than in figures 14(b) and (c), since the turbulence power level is basically 10 decibels greater than the capped-transducer level. (See fig. 14(a).) Also, a comparison of relative areas under the power-spectral-density curves confirms the sequence of Tu_{rms} in figure 13(b).

Figures 14(f) to 14(i) illustrate temporal and spatial variation of the total-pressure power spectral density for selected total-pressure probes on engine 2. Of interest is the noticeably higher power shown in figure 14(h) for probe 5 on rake 4 of engine 2 at the bottom of the duct than for all other engine 2 probes in data set D during climbout. Also, the power level for this probe compares with that of probe 1 on rake 6 of engine 2 (fig. 14(i)) for data sets A, B, and C, but both show powers higher than the bullet-nose probe (fig. 14(f)) and the remaining probe (fig. 14(g)) for all conditions. These observations bring out the apparent nonuniformity of power spectra with position over a compressor inlet.

The spectra for engine 3 probes (figs. 14(d) and 14(e)) compare favorably in shape and overall level with those for comparable probe locations on engine 2 (figs. 14(f) and (g)) except for data set D where higher levels of Tu_{rms} are evidenced at engine 3.

Normalized pressure power spectra for the same sequence of probes as for the takeoff segment are presented in figure 15 for the turbulence-test segment. The power levels for the capped transducer during the turbulence test (fig. 15(a)) are generally higher than those for takeoff (fig. 14(a)), but by less than 5 decibels overall.

The throat static-pressure sensor (see schematic drawing in fig. 2) measured fluctuations in static pressure well upstream of the terminal normal shock. It was located in a region of compression by a complex oblique shock system during the started inlet mode. In figure 15(b), the prominent peak at 160 hertz for data set H and the rise near 200 hertz for data set G are unexplained unless oblique shock impingement or acoustic propagation through the boundary layer was responsible. For stabilized super-sonic conditions in the duct, downstream aerodynamic perturbations cannot propagate forward in the core flow upstream of the normal shock. Thus, as expected, the shapes of the duct static-pressure power curves shown in figure 15(c) are different from those for the throat static-pressure sensor in figure 15(b).

The overall area increases, shown in figures 15(d) to 15(i), which occur between data sets E to H represent increments in Tu_{rms}. The power level decreases more rapidly (about 10 decibels) for probes on engine 3 (figs. 15(d) and 15(e)) at frequencies from about 3 hertz to 40 hertz than for probes on engine 2 (less than 5 decibels), as shown in figures 15(f) to 15(i). The power levels from data set H for engine 2 characterize the flow immediately prior to stall. Thus, figures 15(d) to 15(i) show that the total-pressure power-spectral-density curves for probes at the XB-70-1 inlet exit vary at low frequencies between 10^{-4} and $10^{-5} \times$ 1/hertz and diminish to between 10^{-5} and $10^{-7} \times$ 1/hertz up to 200 hertz at the inlet exit. Also, figures 13(f) and 13(g) show that the areas under these curves represent mean turbulence levels from 14 percent to as high as 31 percent prior to the engine 2 compressor stall.

Comparison of Flight and Wind-Tunnel Data

The turbulence-induced compressor stall may have been first recognized in the wind-tunnel engine-inlet compatibility study described in reference 1, in which a 0.577-linear-scale (one-third-flow-scale) XB-70 inlet modified to fair into a single J93 engine was tested at Arnold Engineering Development Center (AEDC). Stalls were induced during tests at highly supercritical inlet operating conditions by opening the bypass doors (more than 20 stalls at Mach 2.24 to 3.00 were observed), increasing airflow with fixed bypass, and holding the shock at a fixed station and increasing its strength by increasing the sectional area at the station.

Table III summarizes the data taken during the AEDC wind-tunnel tests prior to stalls at Mach numbers from 2.24 to 2.83. Flight data from data set H in table II are also included in table III and agree reasonably well with the wind-tunnel data. The range of turbulence values shown for the flight tests is slightly higher than might have been expected by interpolating between the wind-tunnel values. The upward trend of toler-ance to turbulence with decreasing engine corrected speed in the model data is signi-ficant. This parallels the higher stall margins for lower corrected speeds observed during the wind-tunnel tests. (See ref. 1.)

16

TABLE III.— COMPARISON OF TEST CONDITIONS PRIOR TO STALL EXPERIENCED IN FLIGHT AND FOR THE 0.577-SCALE WIND-TUNNEL MODEL

Mach number, M	Corrected speed, $N/\sqrt{\theta}$	Turbulence, Tu, percent	Distortion, D, percent	Recovery, η, percent
2.24	0.821	16 to 29	14 to 18	74
2.49*	.775	25 to 39	11.4	65.7
2.63	.751	20 to 37	8 to 24	59 to 61
2.83	.723	23	12	56

*Flight data.

Figure 16 compares the level of turbulence variation with recovery for the Mach 2.5 turbulence-test segment from flight with 0.577-scale wind-tunnel data. The results show a 3- to 10-percent higher overall level for the mean flight Tu_{rms} values than predicted by the wind-tunnel data.

The stalls of the J93 engine during AEDC tunnel testing at conditions where the compressor steady-state stall margin was considered to be adequate inspired a two-part wind-tunnel investigation to study in detail the effects of turbulent flow on stall margin. The first phase involved development of a venturi system with a variable-position aerodynamic centerbody connected to a straight-pipe engine airflow simulator which could generate turbulence of a known level and frequency spectrum by using a terminal shock. The simulator, instrumentation, and measured resultant flow field are described in detail by Kimzey in reference 17. The second phase (ref. 2) was concerned with subjecting a J93 engine to well-defined, highly turbulent inflow. Determination of engine operational limits and evaluation of the extent of decrease of stall margin with increasing turbulence were among the objectives.

Data from Kimzey's wind-tunnel simulation for Mach 2.50, a distortion of 11 percent, and a mean turbulence of 16 percent predict a marginal situation near stall. A higher mean turbulence would result in a compressor stall, according to the data. Data are also presented for Mach 2.6, a distortion of 30 percent, and a mean turbulence of 29 percent, which represent maximum simulator turbulence output.

Figure 17 is a schematic drawing of a J93 compressor face showing the location of Kimzey's high-response instrumentation relative to that on engine 2 of the XB-70-1 airplane.

Pressure power spectra from data set E are replotted in figure 18 to permit a spatial comparison with wind-tunnel turbulence-simulation data recorded by Kimzey prior to stall in the 0- to 100-hertz frequency range. The wind-tunnel data represent two simulated flight Mach numbers, M_∞ = 2.2 and 2.6, and average turbulence levels of 16 percent and 19 percent, respectively; the flight data were taken at M_∞ = 2.5 and represent an average turbulence level of 13.7 percent. From 3 to 40 hertz, the spectra from the wind tunnel are significantly higher by an average of about 5 decibels than those from flight, but the agreement is good in the 40- to 100-hertz range.

The wind-tunnel pressure power spectra of figure 18 are compared in figure 19 with flight spectra from data set H, which represent an average Tu_{rms} of 31.2 percent prior to stall of engine 2. In contrast to the preceding figure, the wind-tunnel spectra are in closer agreement with, but slightly below (1 to 2 dB), those from flight in the 3- to approximately 40-hertz range. Above 40 hertz, the wind-tunnel data drop below the comparable flight data.

The differences in spectral shapes between wind-tunnel and flight data in the preceding two figures may be explained partially in terms of Reynolds number differences. Reynolds number is indicative of the relative importance of the inertia and viscous forces in the flow (see, for example, ref. 18), since it can be derived from a ratio of the inertia force and friction, or viscous, force.

Because turbulence propagation distance depends on inertia, and turbulence attenuation on viscosity, the differences in spectral shape between the flight and wind-tunnel curves may be due to the differences in viscous damping in the two flows during transmission from the shock to the compressor face. For the lower Reynolds numbers experienced in tunnel testing, the viscous forces are greater in comparison to the inertial forces than for the flight Reynolds numbers. Kimzey points out that turbulence damping is actually dependent on particle velocity as well as viscosity, and, therefore, attenuation due to viscous effects will be higher at higher frequencies corresponding to increased particle velocities. Hence, it is to be expected that, because of lesser viscous damping more pressure power will be transported to the compressor face at the higher flight Reynolds numbers and that the difference should be most prominent for the higher frequencies. This is confirmed by the results in figure 19.

The higher amplitudes in the low-frequency range, exhibited by the spectra from both the wind-tunnel and the flight tests, give evidence of what Kimzey refers to as "secondary shock oscillation." This low-frequency contributor results from "pumping" of the entire flow field at the resonance frequency of an equivalent Helmholtz resonator including the mass and volume of air between the terminal shock and compressor face.

The engine 2 compressor stall experienced during the XB-70-1 flight was evidently what Kimzey terms "drift-type"; that is, it occurred while the inlet was set at a fixed high turbulence level after an interval that was sufficiently long to allow the flow to deteriorate enough to precipitate stall. This may be differentiated from the "instantaneous stall," which results from a slow, continuous increase in turbulence, producing stall at some point. This is not to say, of course, that the XB-70-1 stall resulted from turbulence alone. On the contrary, the data presented do not provide enough information to determine whether the stall was induced by turbulence or steady-state distortion. What the results imply is a complex combination of distortion and turbulence referred to as dynamic distortion. It should be emphasized that the total-pressure turbulence at a particular probe represents only the axial component of the fluctuations in local air total pressure. This is by no means a complete description of the local flow, since directional fluctuations can contribute significantly to the stall characteristics of an engine.

CONCLUDING REMARKS

Flight-test data were recorded on a flight of the XB-70-1 airplane during takeoff and immediately prior to a compressor stall at Mach 2.5 and an altitude of 63,100 feet (19,200 meters). The data, which were obtained from a limited number of high-response pressure probes in the left inlet, were compared with results from wind-tunnel tests.

The turbulence-producing mechanism in the XB-70-1 inlet appeared to be a strong shock wave interacting with the boundary layer in the region of the throat, which produced an unsteady flow disturbance at the compressor-face plane. The severity of this disturbance varied directly with shock strength (inversely with recovery) for stabilized conditions at Mach 2.5 when measured by a turbulence factor defined herein.

The inlet turbulence problem may be analyzed by using random data-analysis techniques, since the assumptions of stationarity, randomness, and normality were found to be approximately valid for the XB-70-1 inlet pressure data.

During takeoff of the XB-70-1 airplane, a mean turbulence level as high as 12 percent was experienced at the left-inlet exit. The level tended to decrease slightly as the velocity of the airplane increased, apparently due to a decrease in the flow separation occurring at the entrance to the sharp-lip inlet.

For flight Reynolds numbers (based on duct height) of about 8.6×10^6 for a large, started, two-dimensional, mixed-compression inlet, the normalized total-pressure power-spectral-density curves derived from measurements at the inlet exit varied at low frequencies between 10^{-4} and $10^{-5} \times$ 1/hertz and diminished to between 10^{-5} and $10^{-7} \times$ 1/hertz up to 200 hertz. The areas under these curves represented mean turbulence levels from 14 percent to as high as 31 percent prior to compressor stall at Mach 2.5.

Comparison of flight and wind-tunnel data indicated that the flight-inlet turbulence-producing mechanism can be simulated successfully in ground-test facilities for engine testing purposes up to at least 40 hertz. Above 40 hertz, Reynolds number effects are apparent in the diminished wind-tunnel pressure-wave power spectrum. As a result, higher turbulence values were experienced in flight than in the wind tunnel by an engine compressor prior to stall.

Flight Research Center,
National Aeronautics and Space Administration,
Edwards, Calif., January 9, 1970.

REFERENCES

1. Martin, Arnold W. ; and Kostin, Leonard C. : Propulsion System Dynamic Tests Results. North American Aviation, Inc. (NASA CR-73114), 1967.

2. Kimzey, W. F. : An Investigation of the Effects of Shock-Induced Turbulent Inflow on a YJ93-GE-3 Turbojet Engine. AEDC-TR-66-198, Arnold Eng. Dev. Center, Nov. 1966.

3. Mechtly, E. A. : The International System of Units - Physical Constants and Conversion Factors. NASA SP-7012, 1964.

4. Wolowicz, Chester H. ; Strutz, Larry W. ; Gilyard, Glenn B. ; and Matheny, Neil W.: Preliminary Flight Evaluation of the Stability and Control Derivatives and Dynamic Characteristics of the Unaugmented XB-70-1 Airplane Including Comparisons With Predictions. NASA TN D-4578, 1968.

5. Gallagher, Robert J. : Investigation of a Digital Simulation of the XB-70 Inlet and Its Application to Flight-Experienced Free-Stream Disturbances at Mach Numbers of 2.4 to 2.6. NASA TN D-5827, 1970.

6. Raymes, F. ; and Ball, W. : XB-70 Air Induction System Geometric and Area Requirements. Rep. No. NA59-1045, North American Aviation, Inc. , June 26, 1959 (rev. 1961).

7. Wolfe, J. E. : Propulsion System Performance Substantiation Report for the XB-70A Air Vehicle (YJ93-GE-3 Engines). Rep. No. NA-64-674, North American Aviation, Inc. [1964].

8. Smith, Ronald H. ; Bellman, Donald R. ; and Hughes, Donald L. : Preliminary Flight Investigation of Dynamic Phenomena Within Air Breathing Propulsion Systems of Supersonic Aircraft. AIAA Paper No. 68-593, 1968.

9. Edwards, E. L. : An Airborne Data Acquisition System for Use in Flight Testing the XB-70 Airplane. Selected Instrumentation Application Papers From AGARD Flight Mechanics Panel - Twenty-Sixth Meeting, AGARD Rep. 507, June 1965, pp. 23-48.

10. Edwards, E. L. : A Data Processing Facility for the XB-70 Flight Test Program. Flight Test Instrumentation, AGARD Conf. Proc. No. 32, 1967, pp. 243-258.

11. Ince, D. B. : Application Experience With the B-70 Flight Test Data System. Aerospace Instrumentation. Vol. 4 - Proceedings of the Fourth International Aerospace Symposium, College of Aeronautics, Cranfield, Eng. , March 21-24, 1966, M. A. Perry, ed. , Pergamon Press, Ltd. , 1967, pp. 195-208.

12. Nichols, Myron H. ; and Rauch, Lawrence L. : Radio Telemetry. Second Ed. , John Wiley & Sons, Inc. , c.1956.

13. Stiltz, Harry L. , ed. : Aerospace Telemetry. Prentice-Hall, Inc. , 1961.

14. Kostin, Leonard C.; and Millstone, Sidney D.: Application of Statistical Parameters in Defining Inlet Airflow Dynamics. AIAA Paper No. 68-649, 1968.

15. Bendat, Julius S.; and Piersol, Allan G.: Measurement and Analysis of Random Data. John Wiley & Sons, Inc., c. 1966.

16. Burrow, Laurie R., Jr.: Some Analog Methods of Power Spectral Density Analysis. Preprint No. 1.5-3-65, Instr. Soc. Am., Oct. 1965.

17. Kimzey, W. F.: An Investigation and Calibration of a Device for the Generation of Turbulent Flow at the Inlet of a Turbojet Engine. AEDC-TR-65-195, Arnold Eng. Dev. Center, Oct. 1965.

18. Schlicting, Hermann: Boundary-Layer Theory. Sixth ed., McGraw-Hill Book Co., Inc., 1968, pp. 13,14.
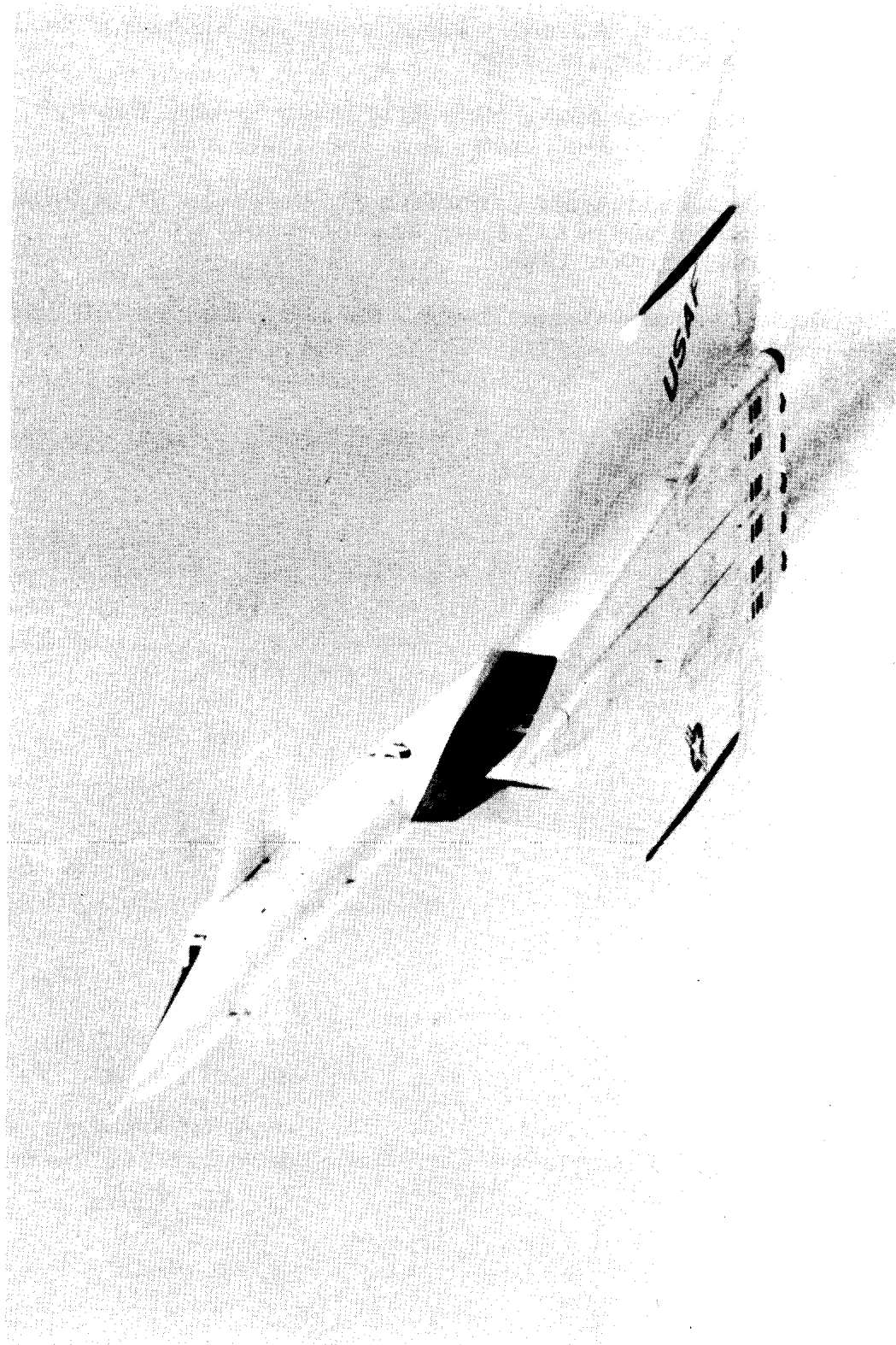
Figure 1.– XB-70-1 airplane.

Top view

Side view
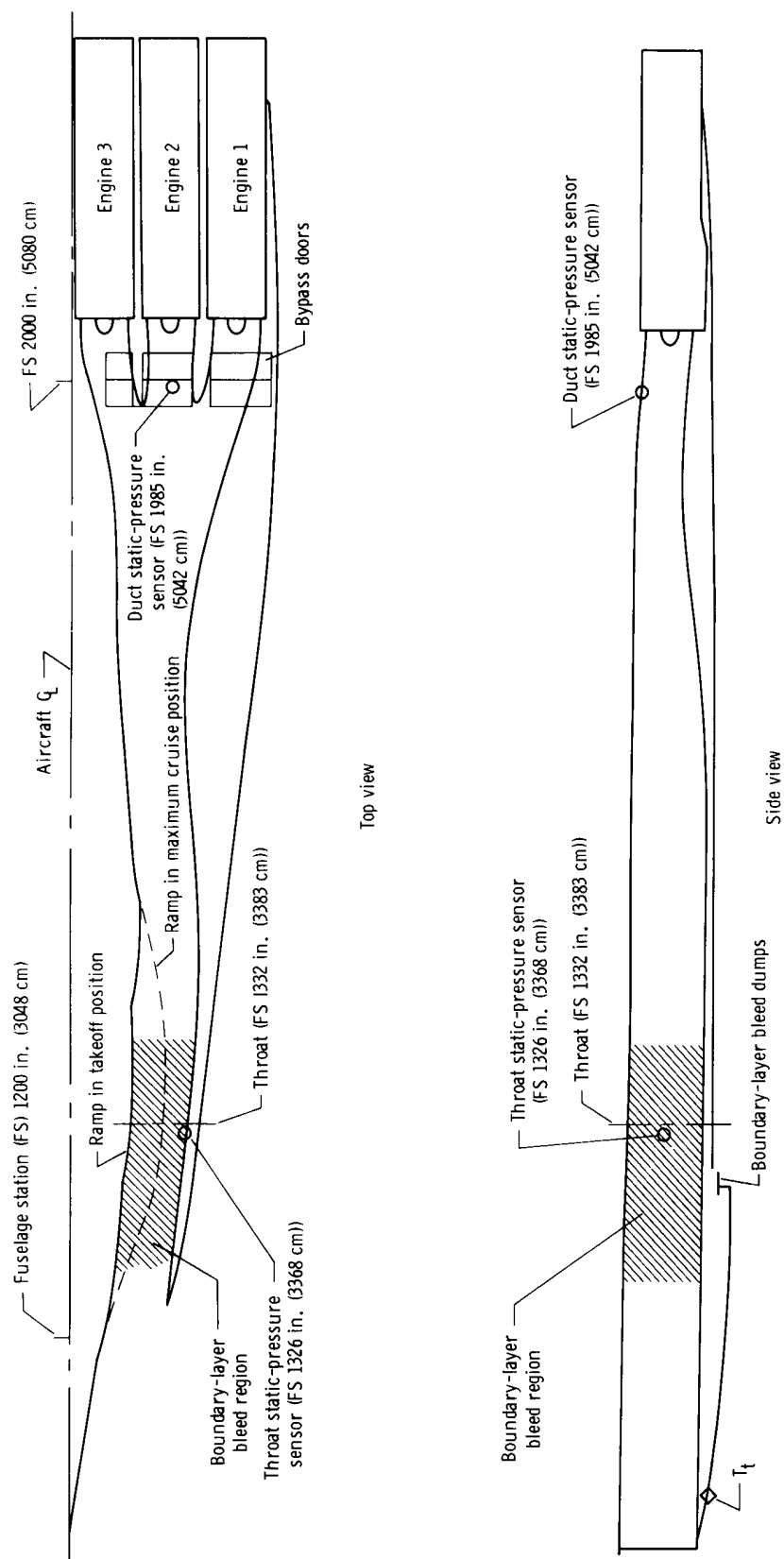
Figure 2. — Left inlet of XB-70-1 airplane.

23

$M_\infty < 1$

Hinge point

$M < 1$

Subsonic

$1 < M_\infty < 2$

$M < 1$

Low supersonic

$M_\infty > 2$

$M > 1$

$M < 1$

Terminal shock location for:

Lower than normal performance, or "supercritical"

Normal performance

High supersonic
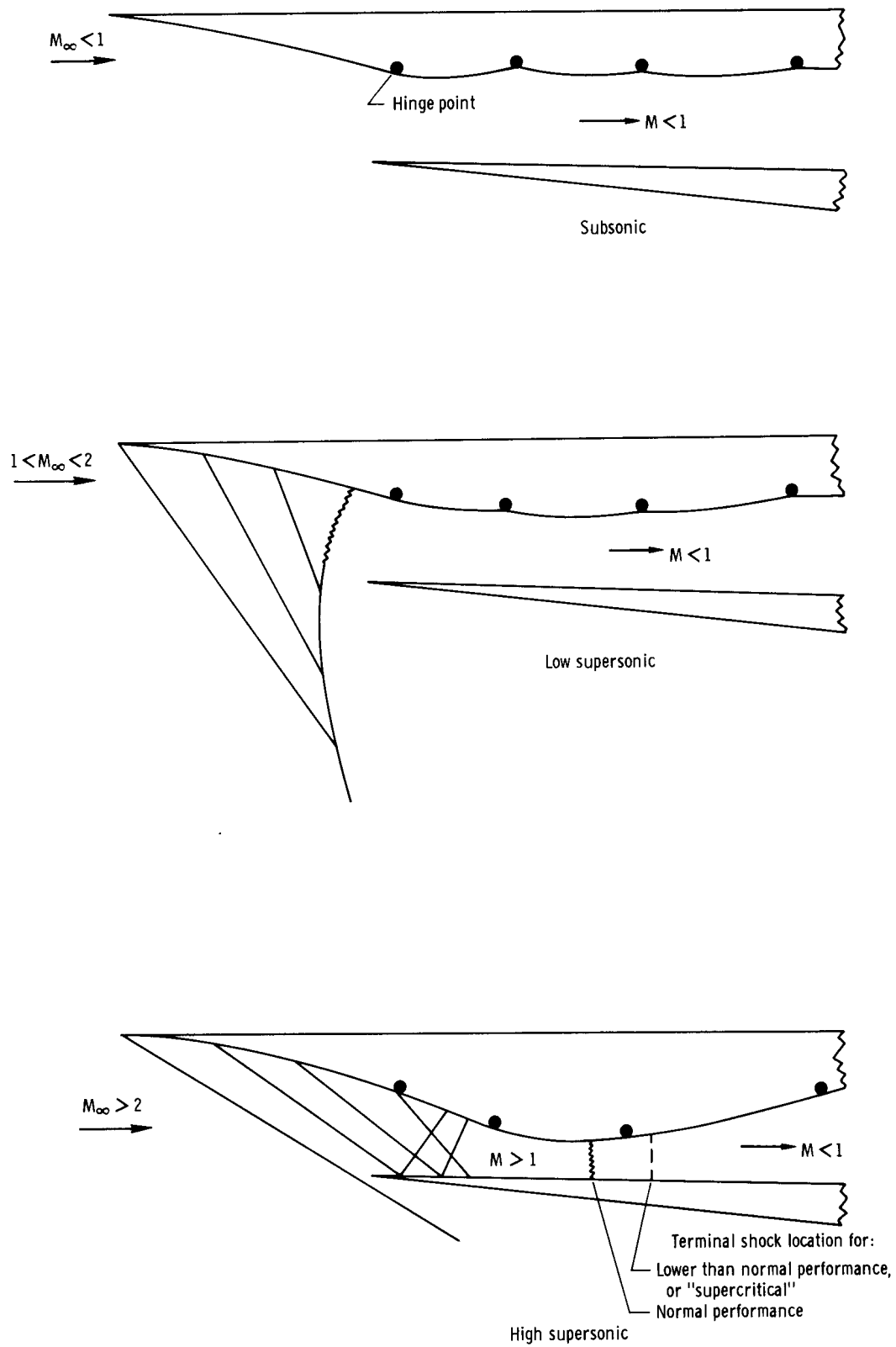
Figure 3. — Three modes of inlet operation.

24
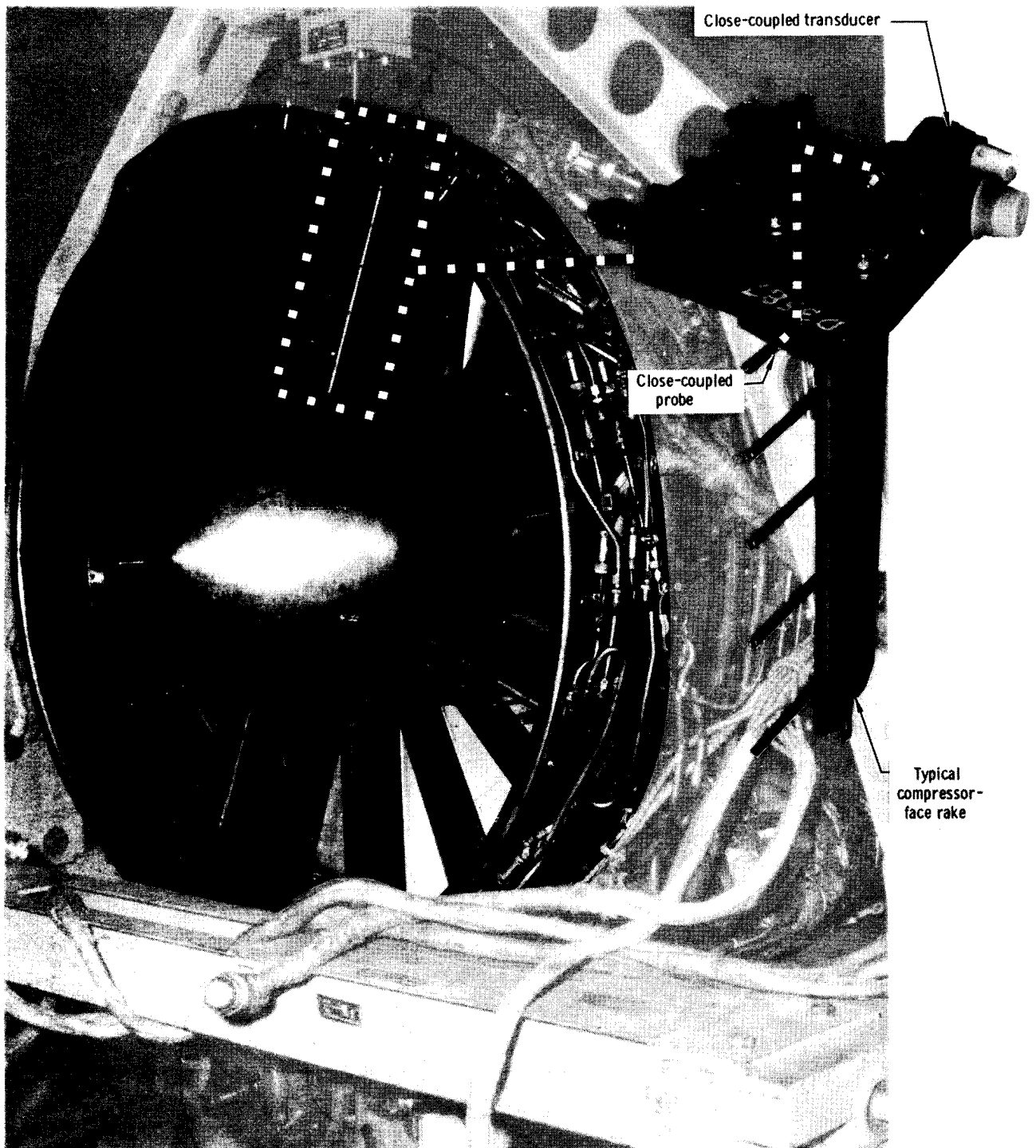
Figure 4.— Compressor face 3 showing close-coupling of typical transducer and probe.

R denotes rake
P denotes probe
○ Dynamic-pressure probe (analog recording)
● Dynamic-pressure probe (analog + digital recording)
□ Low-response-pressure probe (digital recording)
Flags denote probes for which power spectral
densities are presented
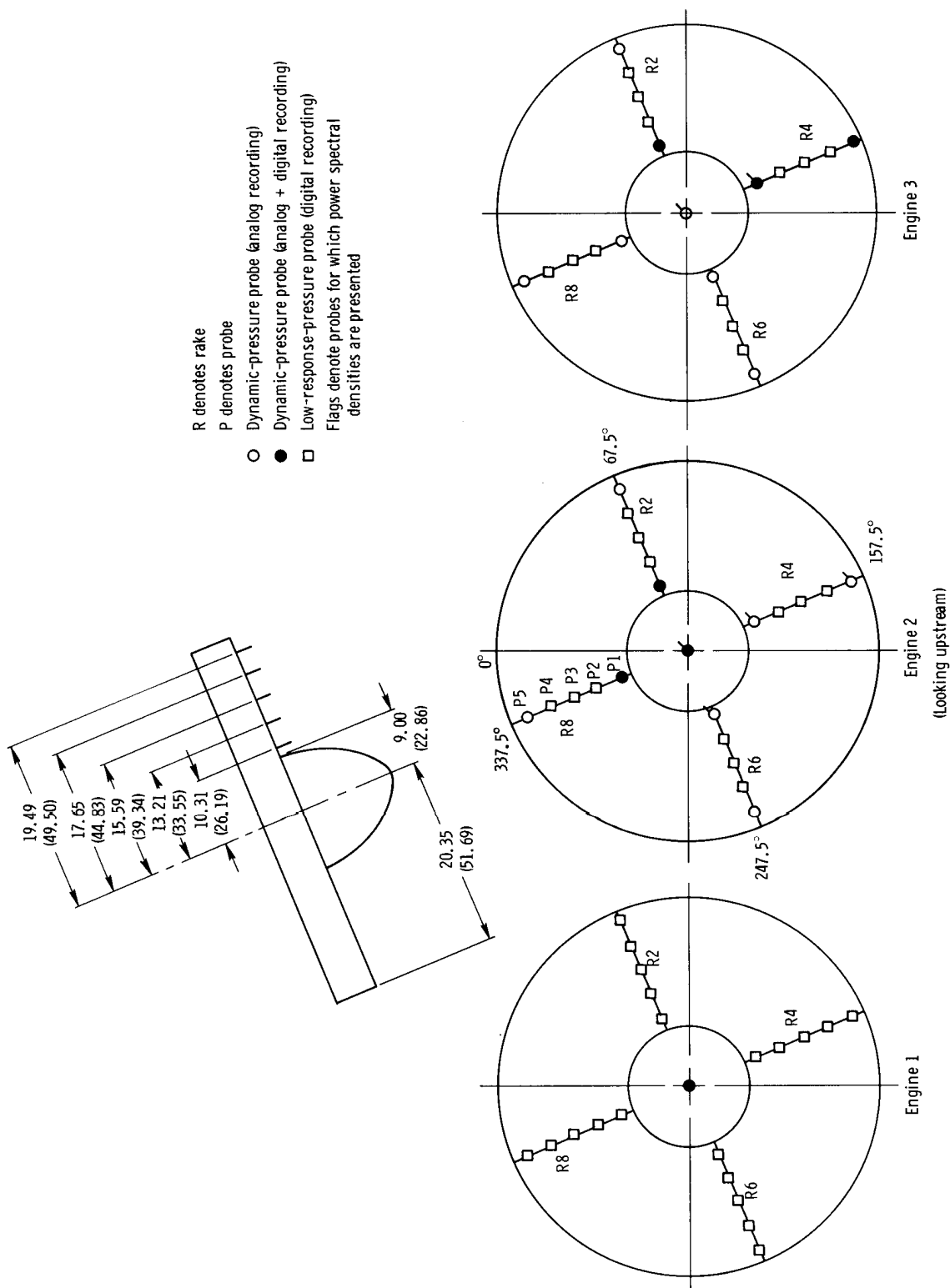
Figure 5.— Compressor-face instrumentation. Not drawn to scale; all dimensions in inches (centimeters) unless otherwise noted.
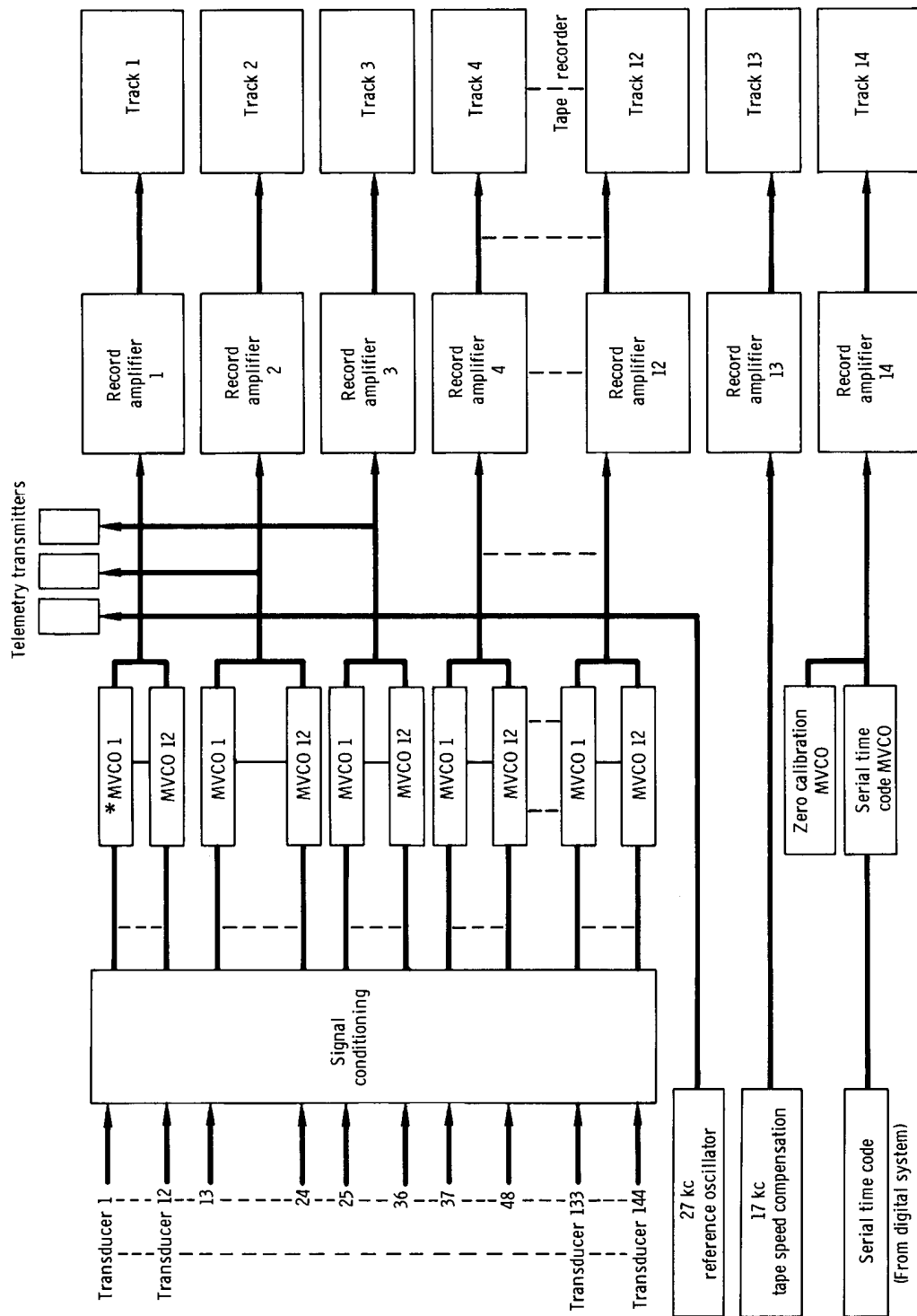
Figure 6. — Analog recording system.

27
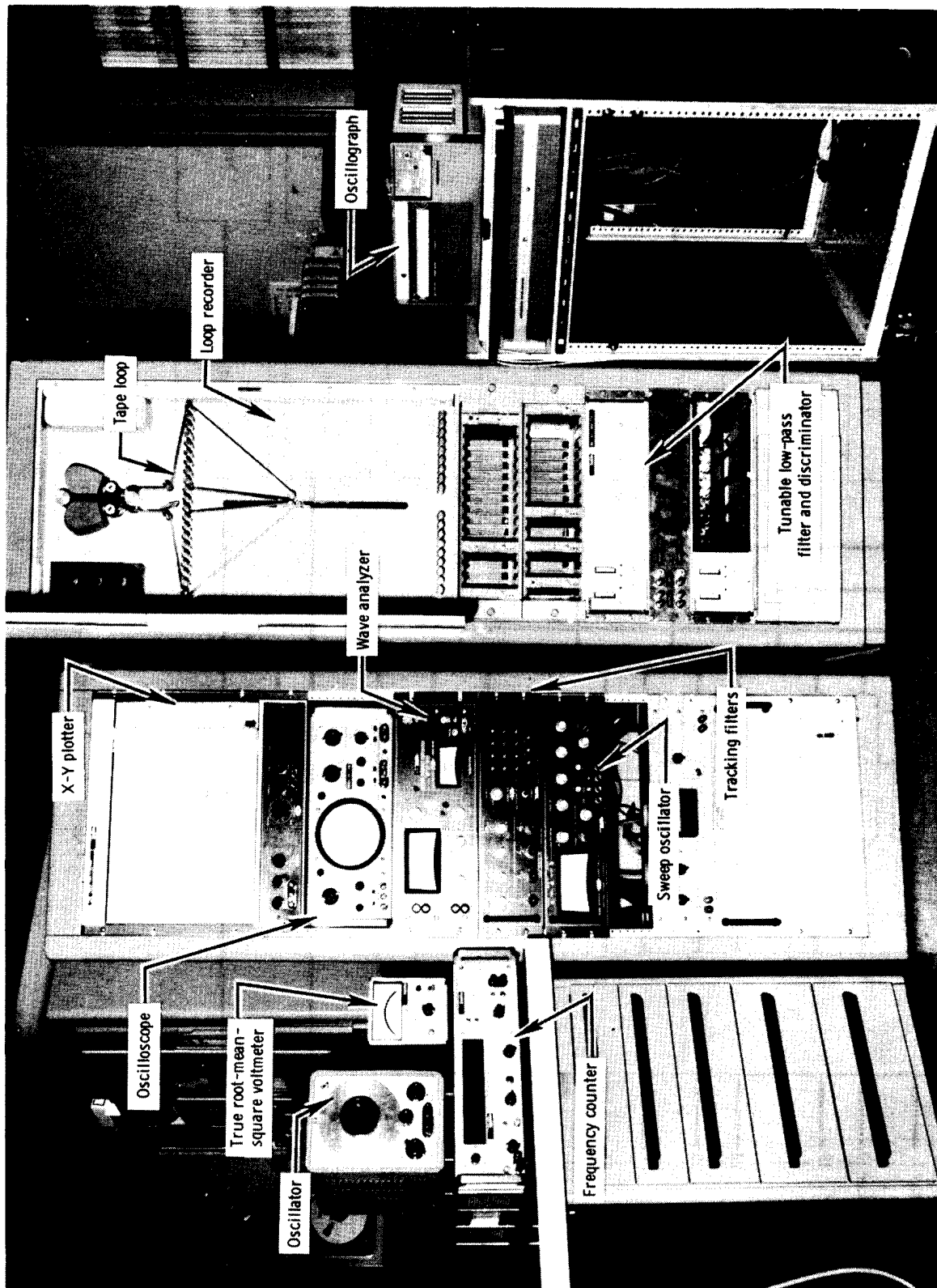
Figure 7. – Analog electronics used in data reduction.
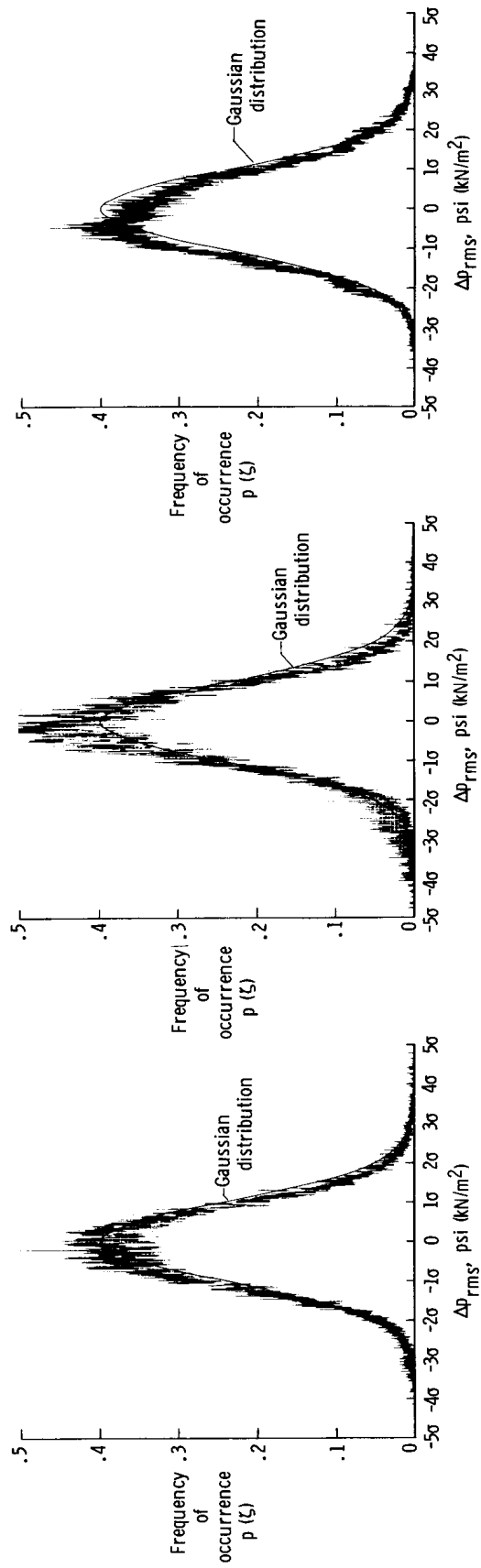
(a) Duct static-pressure probe; $\sigma = 0.17$ psi (1.17 kN/m^2).

(b) Engine 2; capped transducer; $\sigma = 0.07$ psi (0.48 kN/m^2).

(c) Engine 2; bullet-nose total-pressure probe; $\sigma = 0.50$ psi; (3.45 kN/m^2).

Figure 8.— Typical probability-density distributions of flight data for M = 2.5, h = 63,100 feet, (19,200 meters), data set H, $\zeta = p(t)$.

$$Tu_\Delta = \frac{\Delta p}{p_{t_{2_{av}}}}, \quad Tu_{rms} = \frac{6\Delta p_{rms}}{p_{t_{2_{av}}}}$$

$p_{t_{2_{av}}}$ = time and geometrically averaged total pressure

$\Delta p = 6\Delta p_{rms} = 6\sigma$

= peak-to-peak amplitude band of 99.7 percent probability for stationary, normal data

Area proportional to probability that pressure amplitude will occur within 0 and $+\sigma$

Frequency of occurrence $p(\zeta)$

$$p(\zeta) = \frac{1}{\sigma\sqrt{2\pi}} \exp\left(-\frac{1}{2}\frac{\zeta^2}{\sigma^2}\right)$$

where

$\zeta = p(t)$

$$\sigma = \Delta p_{rms} = \sqrt{\frac{1}{\tau}\int_0^\tau (\zeta - \zeta_{av})^2 \, dt}$$

for zero mean $\zeta_{av} = 0$

3σ

2σ

σ

0

$-\sigma$

-2σ

-3σ

$p(t)$

0

Δp

$\Delta p_{rms} = \sigma$

t

Zero mean
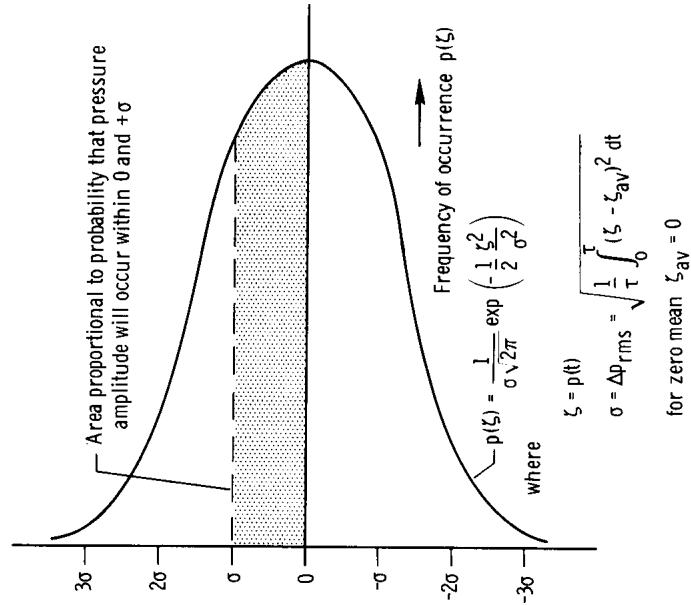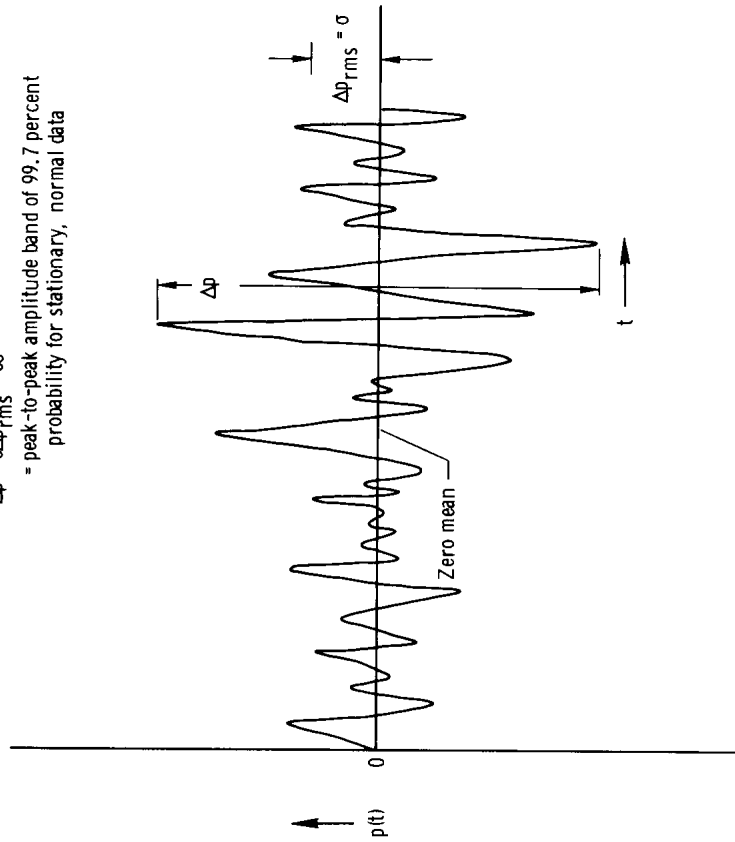
Figure 9. – Pressure waveform amplitude distribution.

30
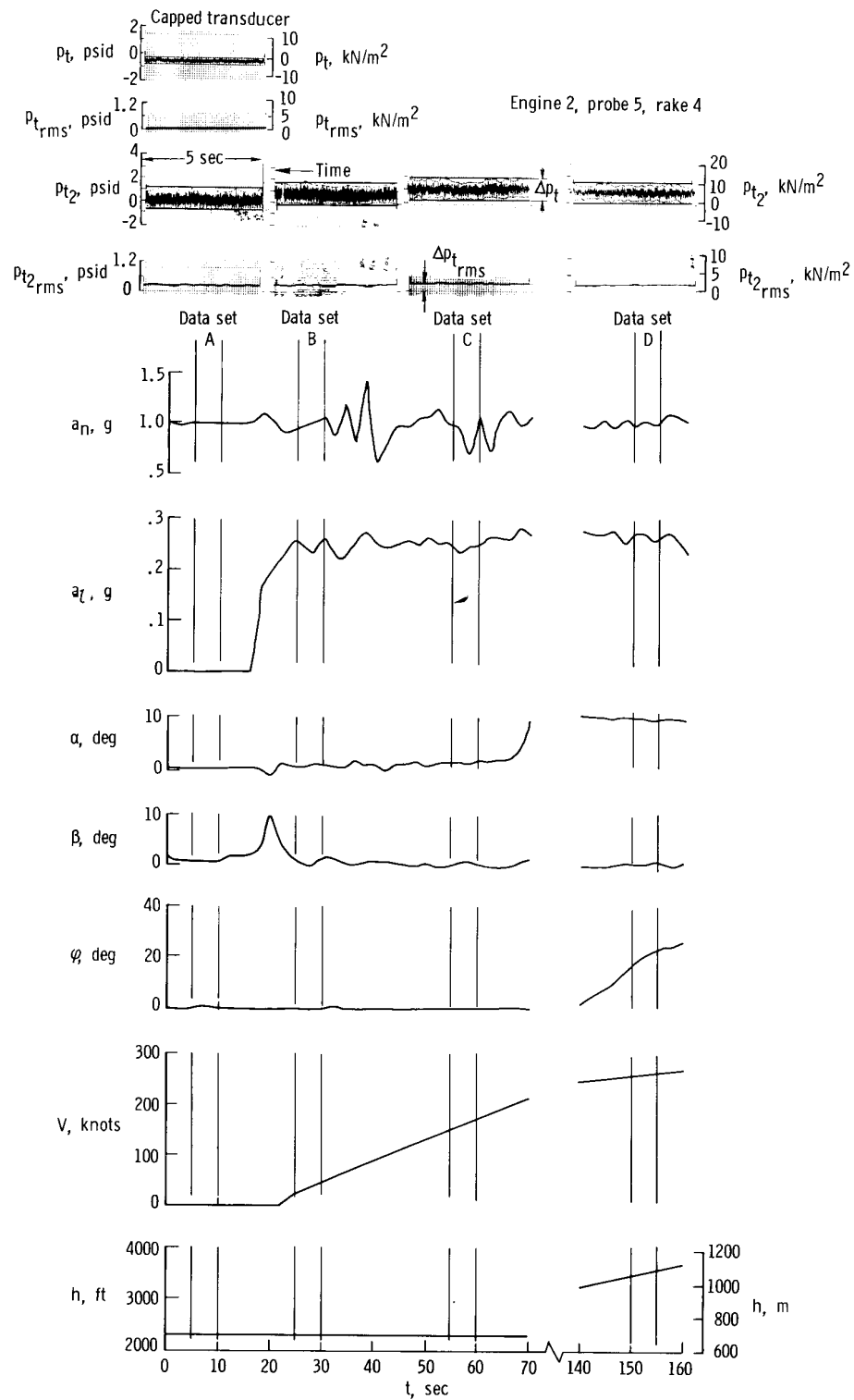
Figure 10. — Data samples and time histories of selected flight parameters during
XB-70-1 takeoff data-set intervals.
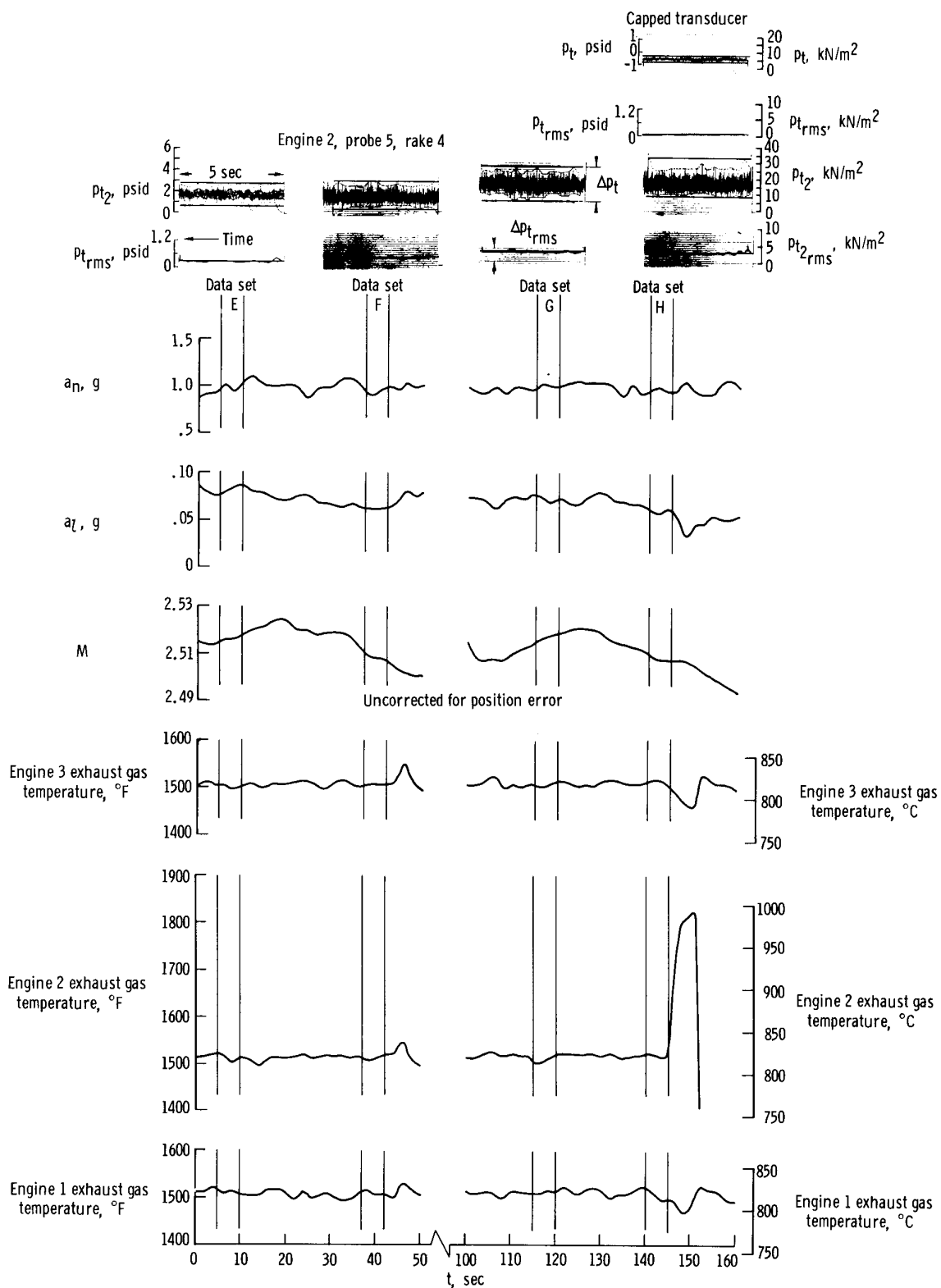
Figure 11.— Data samples and time histories of selected flight parameters during
XB-70-1 Mach = 2.5 turbulence test data-set intervals.

Figure 12. — Comparison between two methods of measuring the turbulence parameter for all probes and conditions. Numbers beside circles denote repeated points.
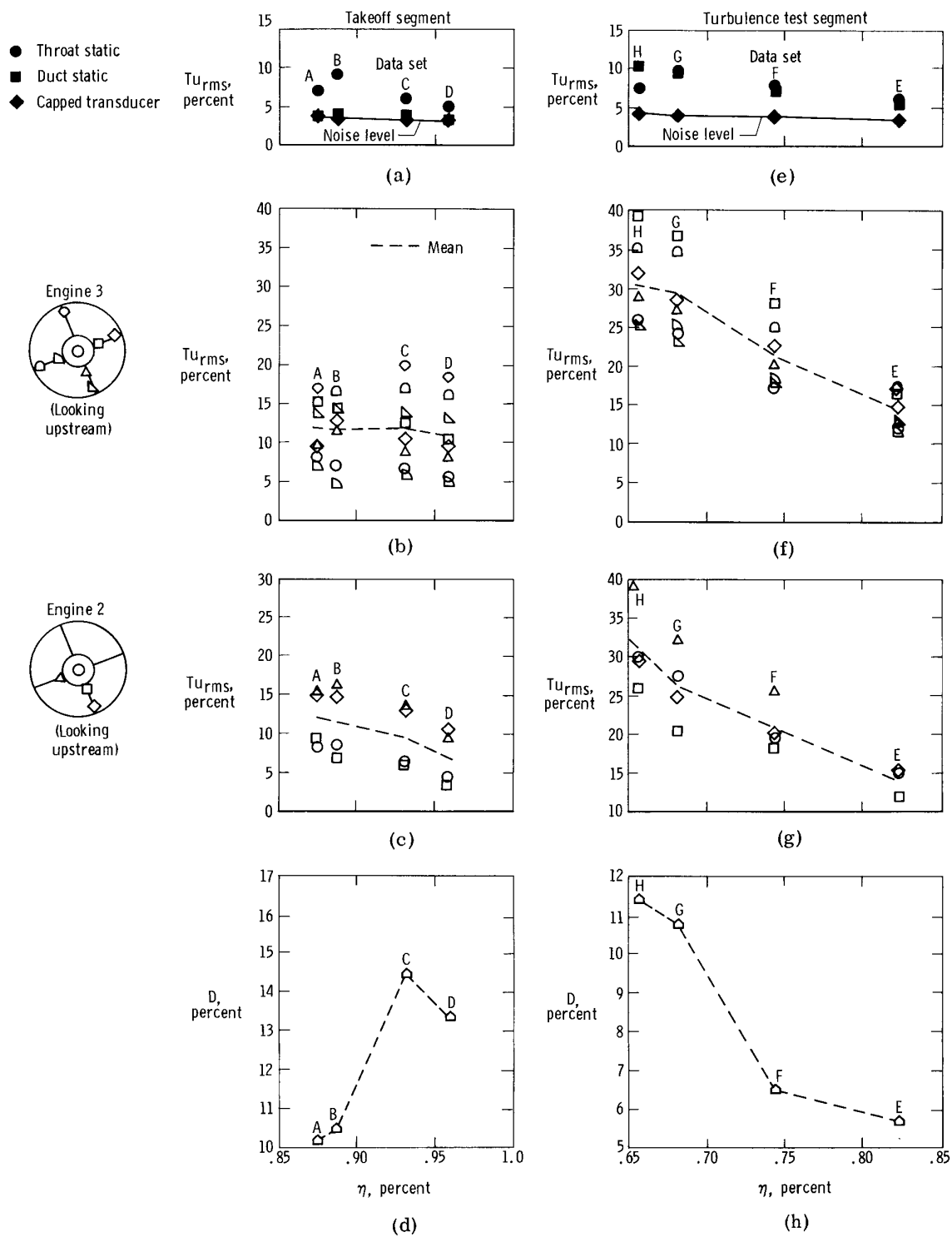
Figure 13.— XB-70-1 static- and total-pressure turbulence and average distortion
during takeoff and turbulence test at M = 2.5, h = 63,100 feet (19,200 meters).
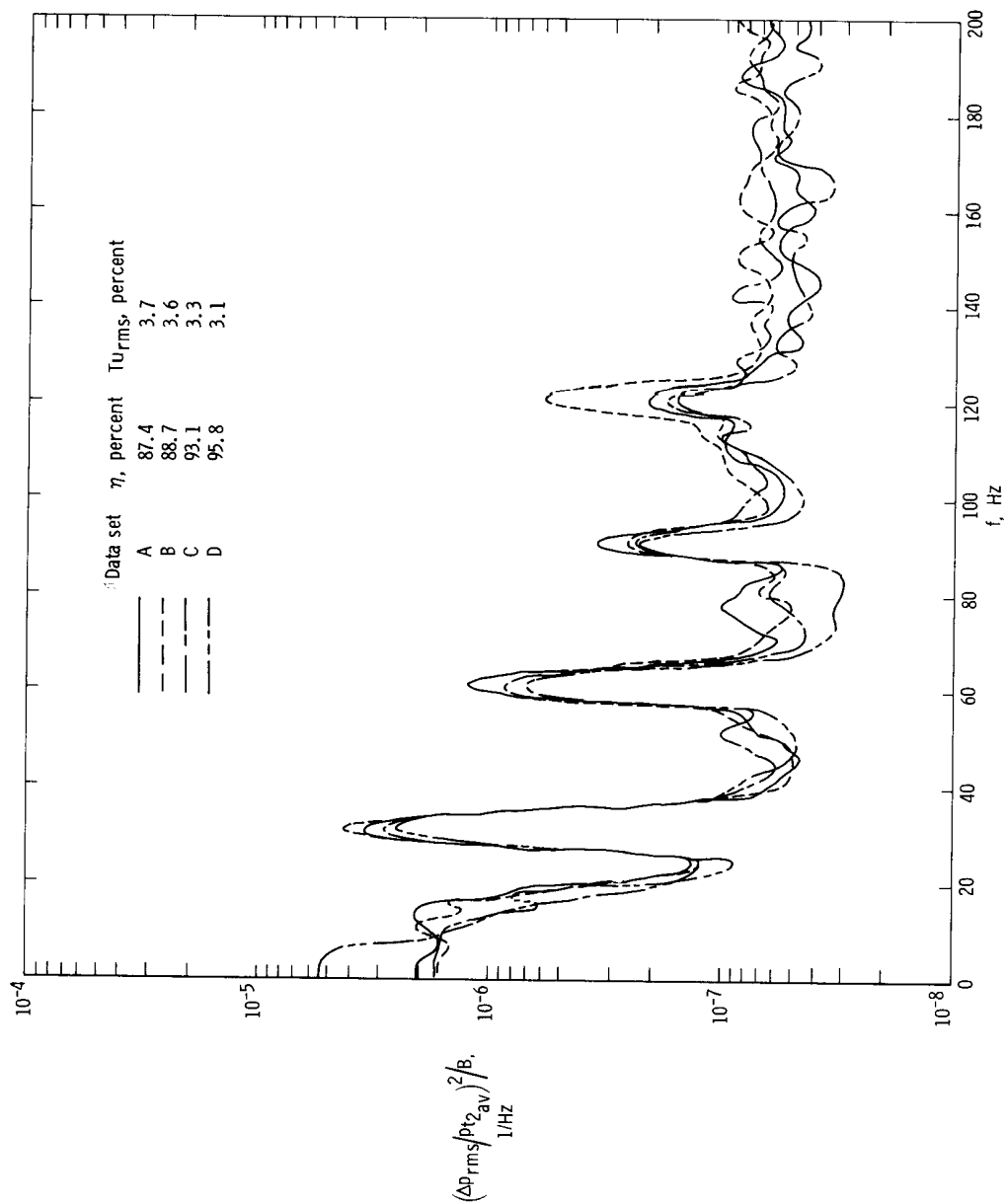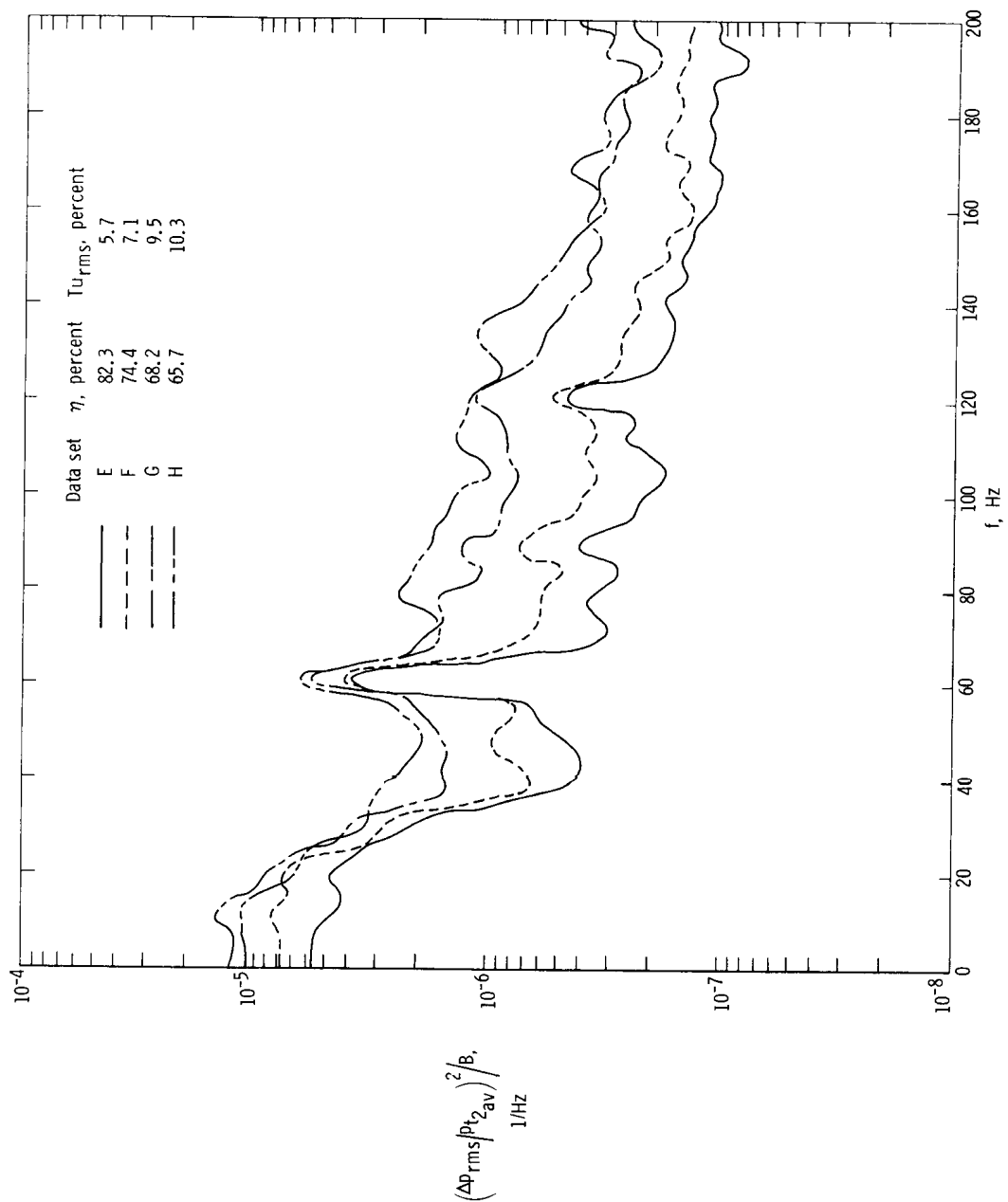
(a) Capped transducer (engine 2).

Figure 14. – Inlet static-pressure and compressor-face total-pressure power spectral densities for takeoff conditions. $n = 50$; $\epsilon = 0.2$; $B = 5$ Hz.
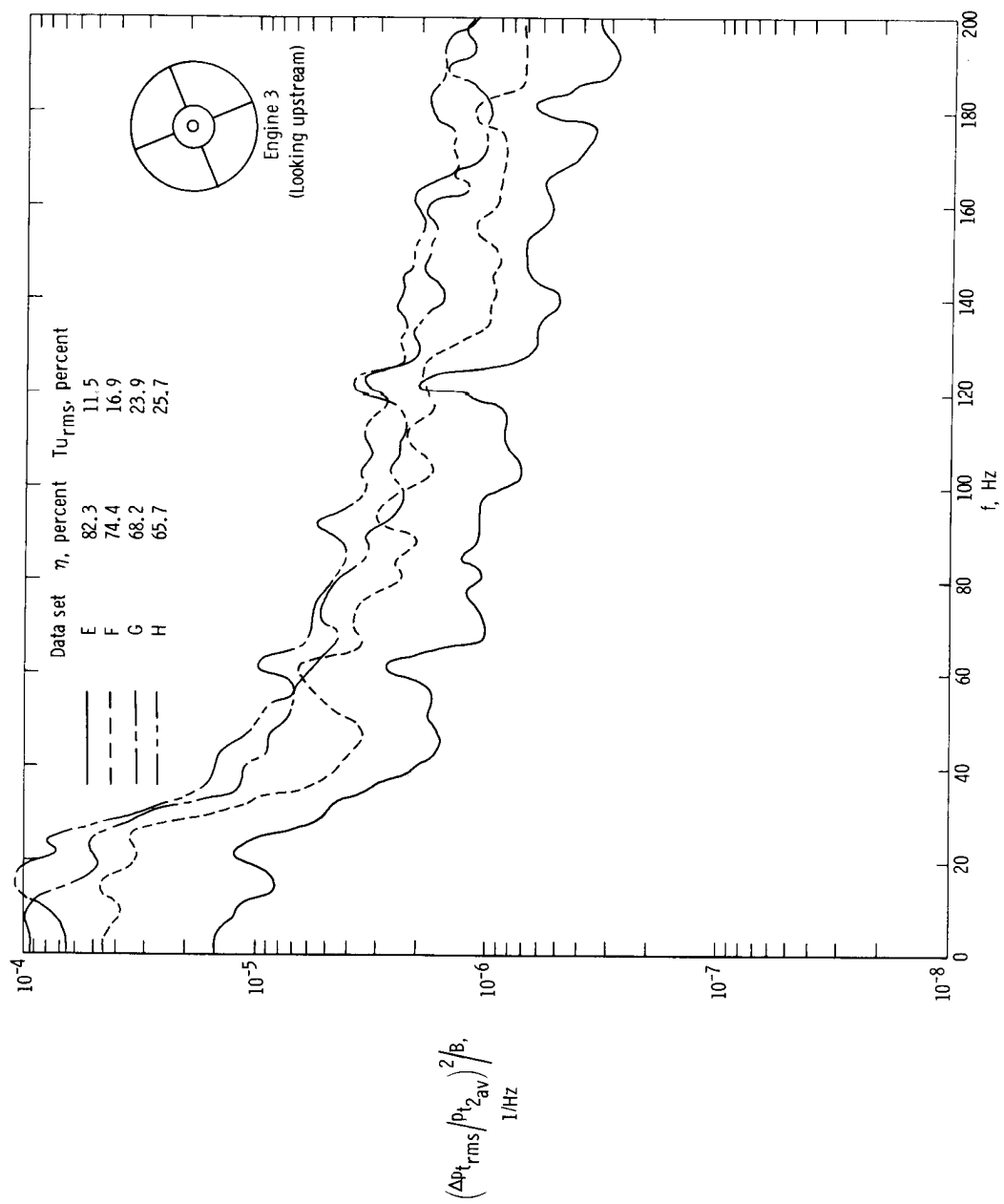
35
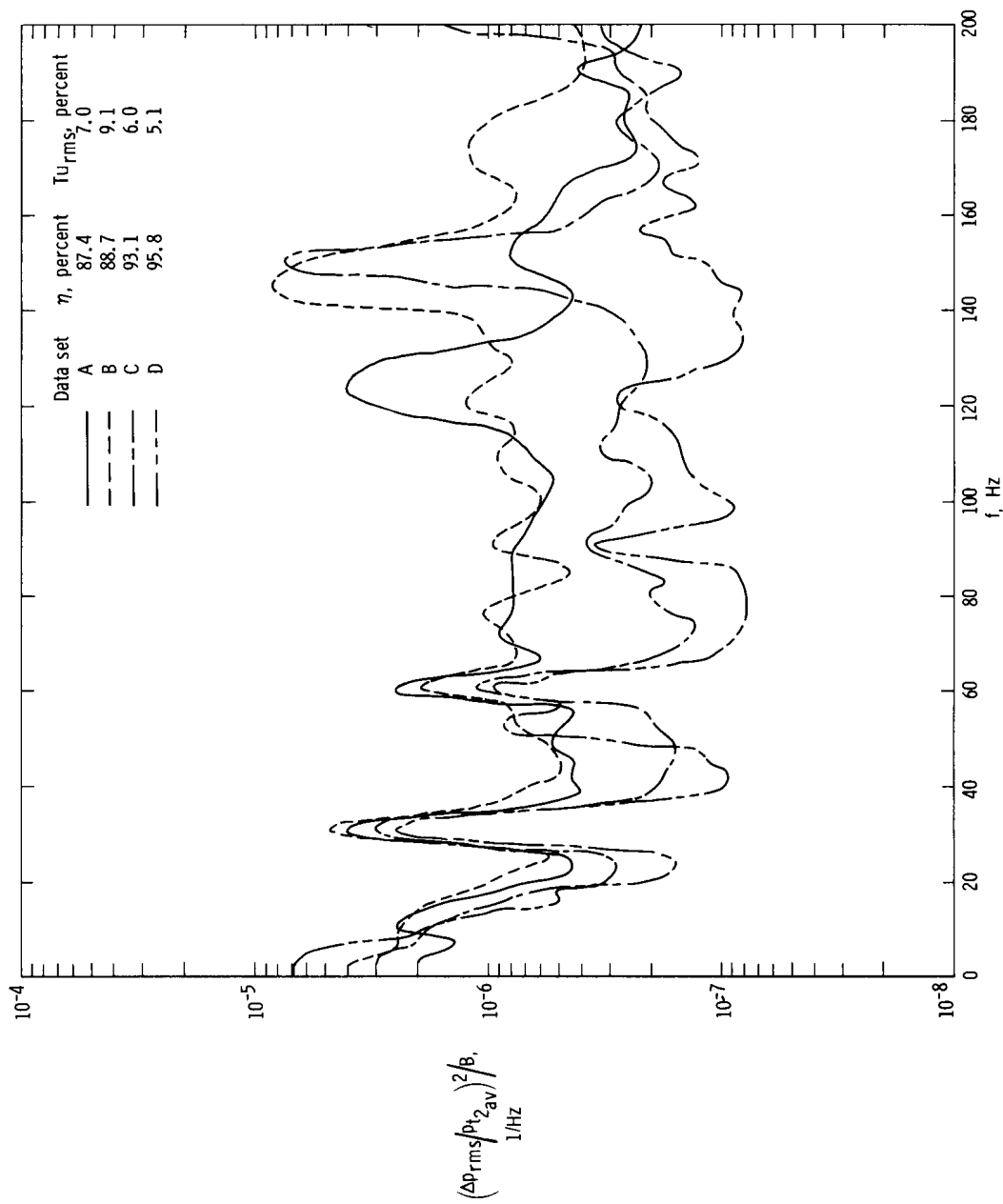
(b) Throat static-pressure sensor.

Figure 14. – Continued.

(c) Duct static-pressure sensor.

Figure 14. – Continued.

Data set	η, percent	Tu_{rms}, percent
A	87.4	8.1
B	88.7	7.0
C	93.1	6.4
D	95.8	5.5

Engine 3
(Looking upstream)

$\left(\Delta p_{t_{rms}} / p_{t_{2_{av}}}\right)^2 / B$, 1/Hz
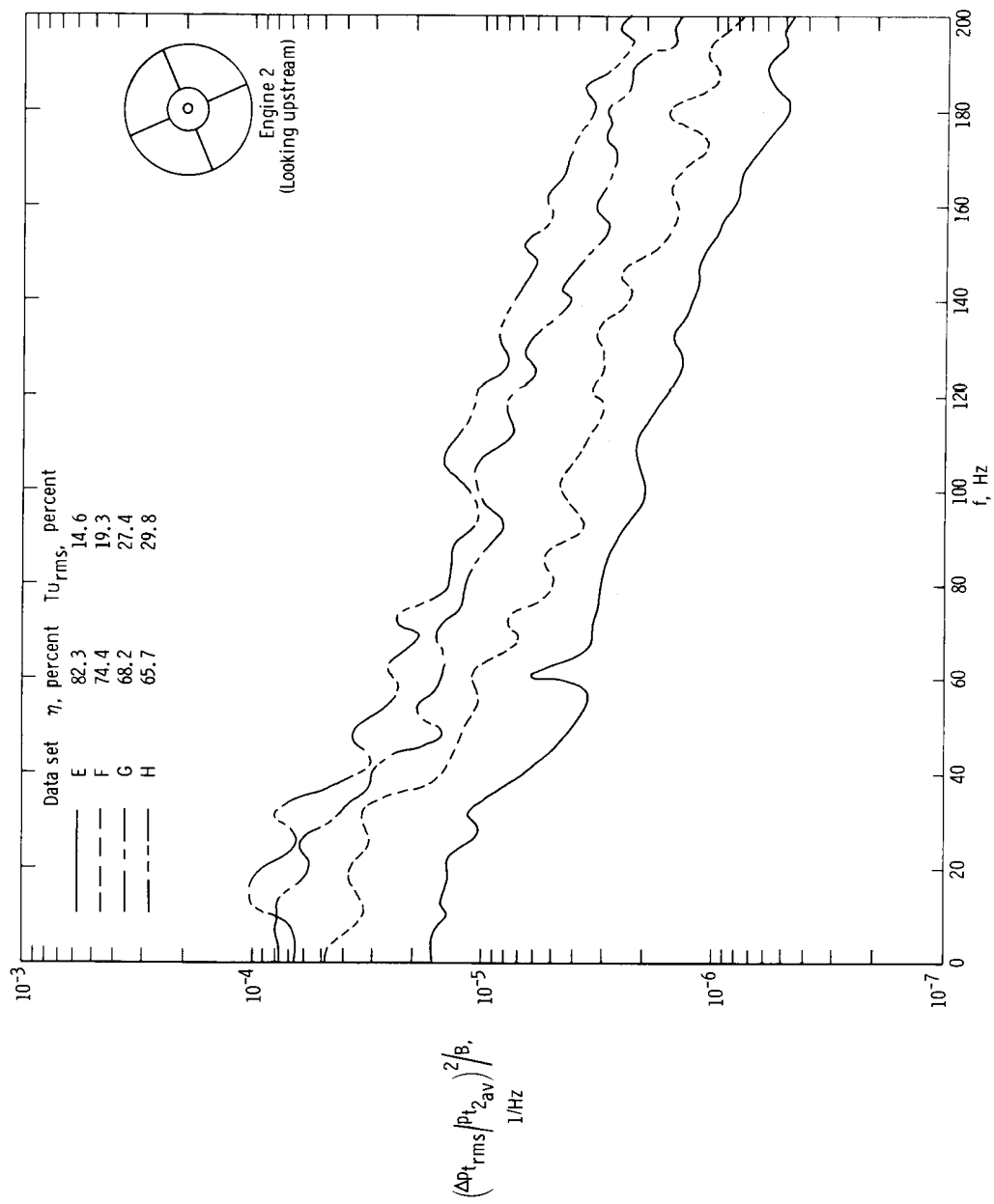
f, Hz
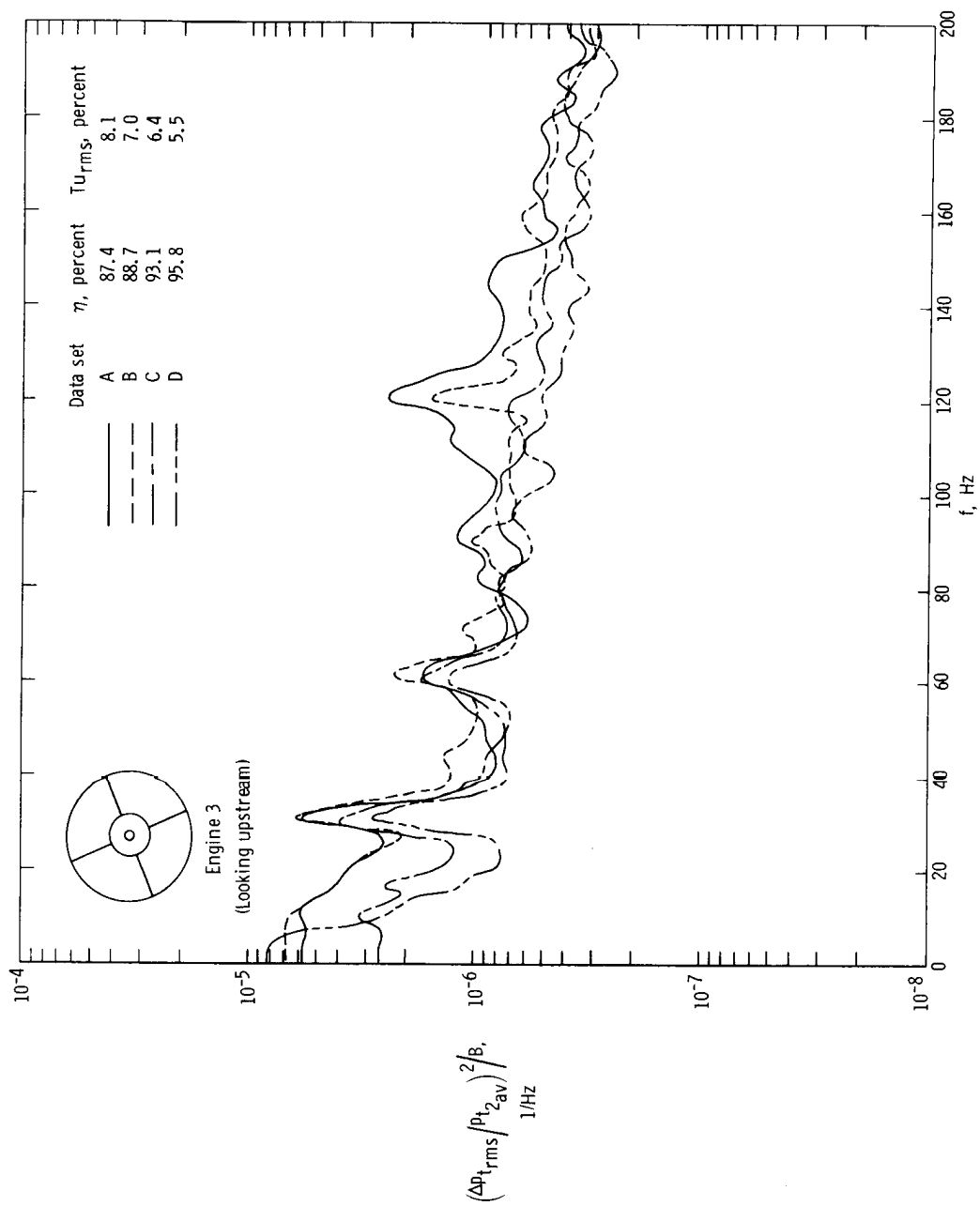
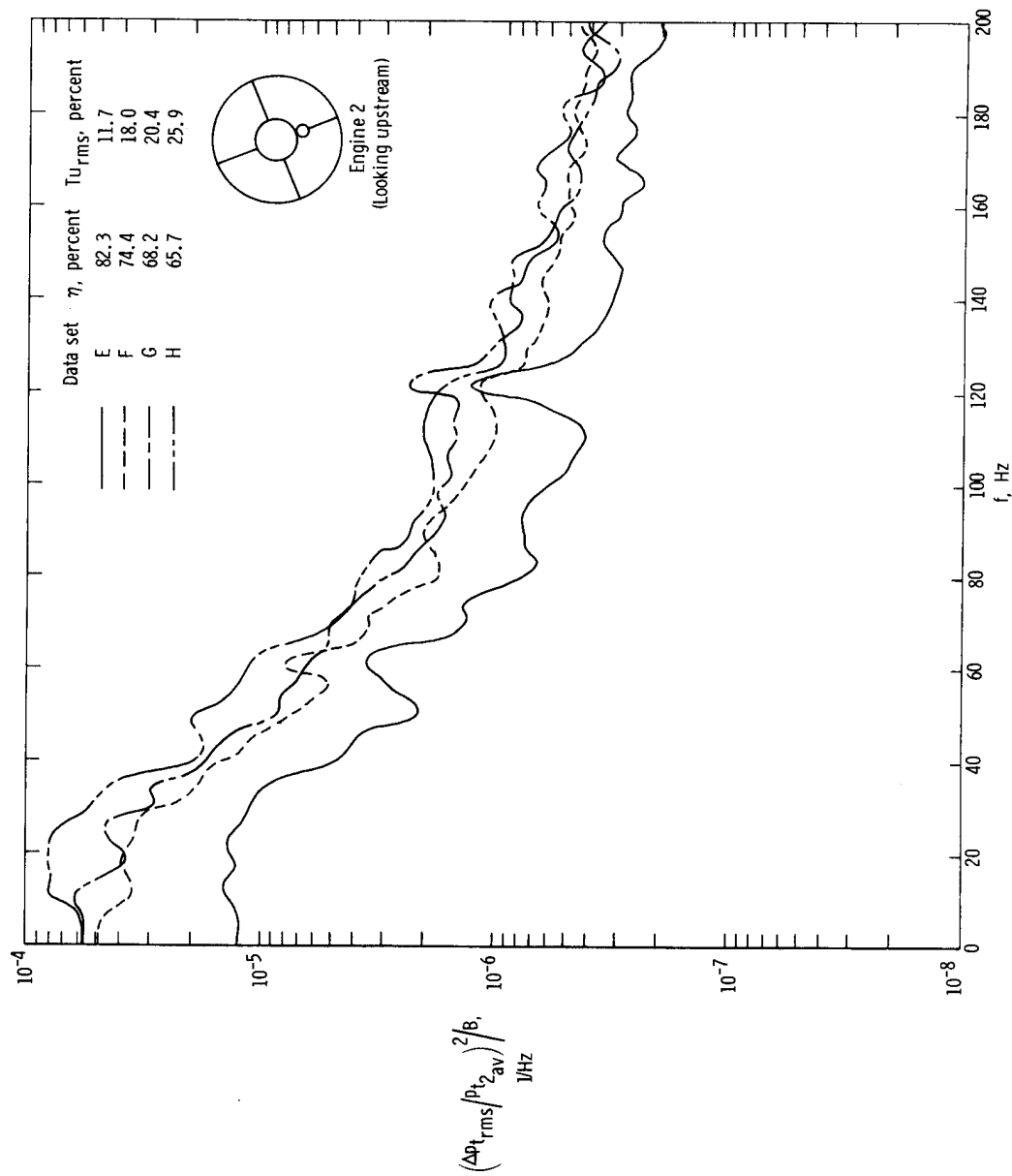(d) Engine 3; bullet-nose total-pressure probe.

Figure 14. – Continued.

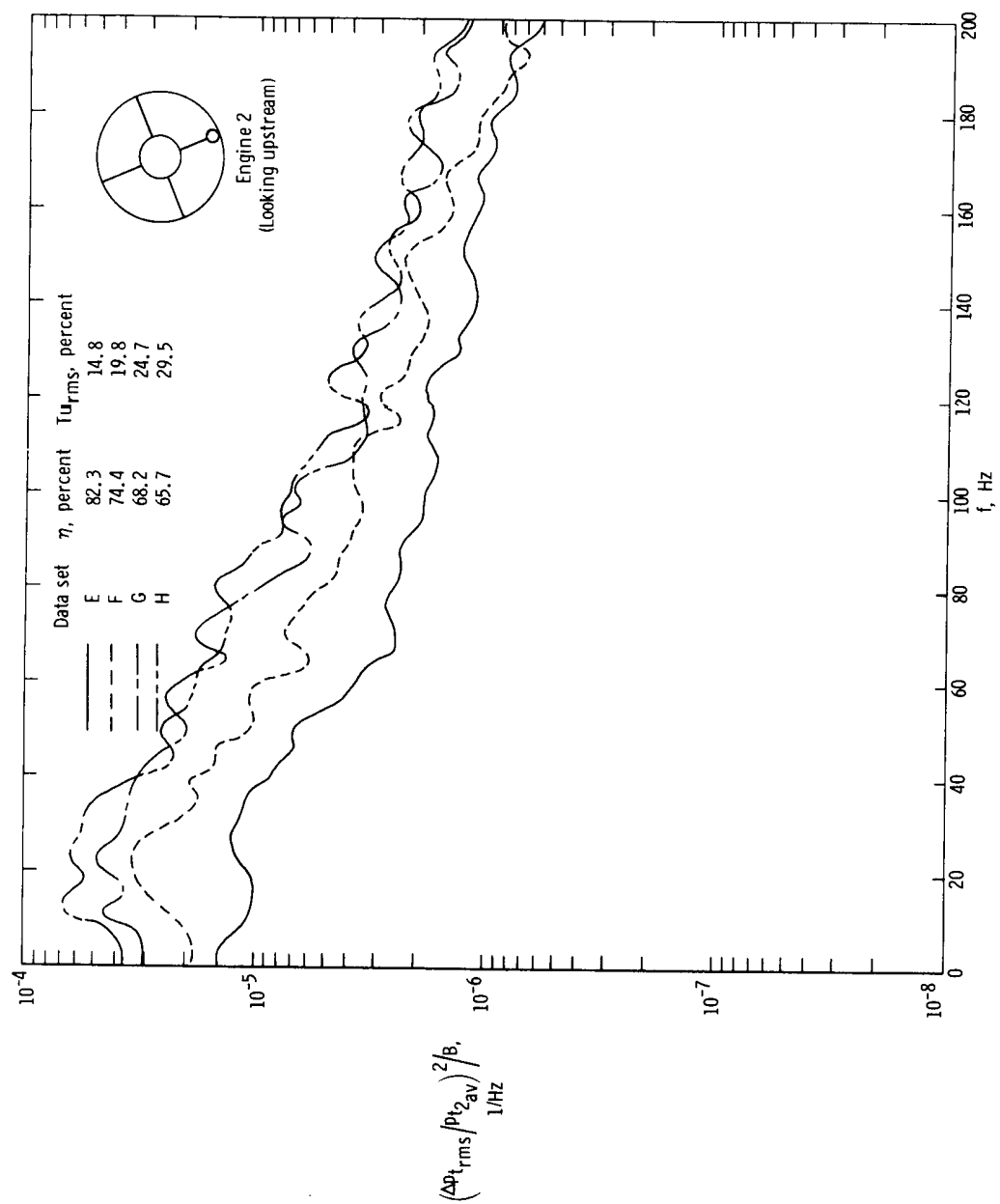(e) Engine 3; rake 4; total-pressure probe 1.

Figure 14. – Continued.

39
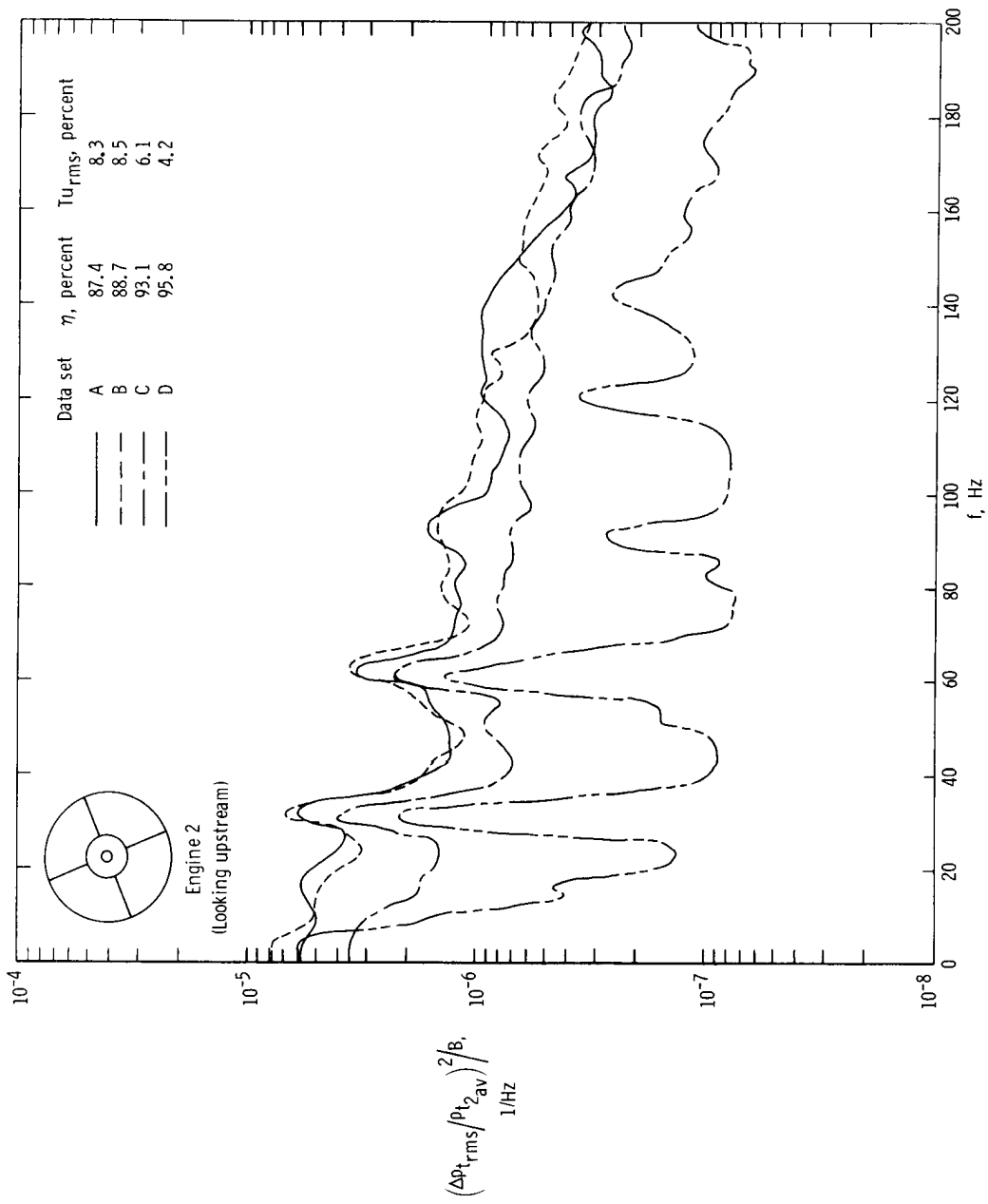
(f) Engine 2; bullet–nose total–pressure probe.

Figure 14.– Continued.
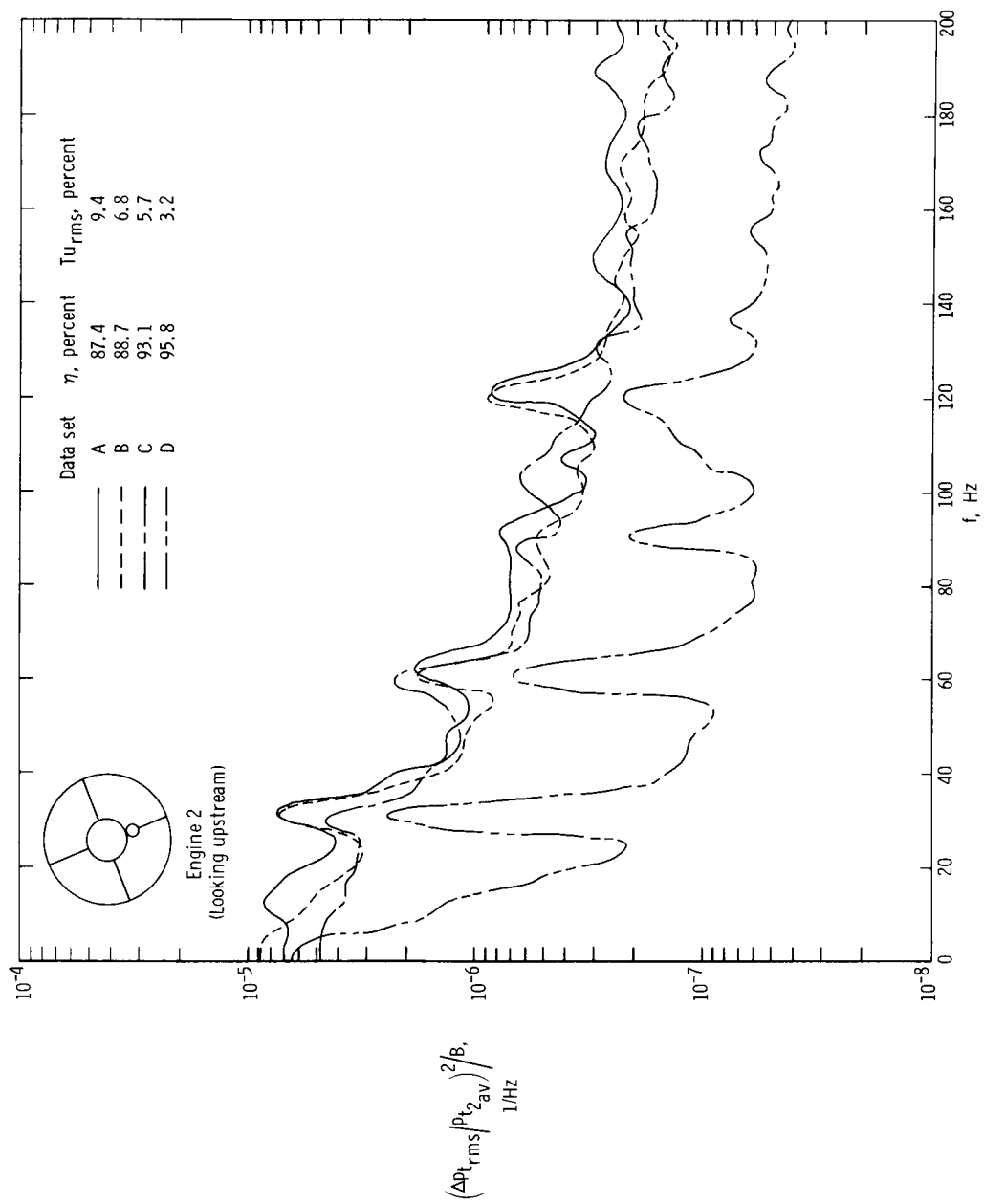
(g) Engine 2; rake 4; total-pressure probe 1.

Figure 14. – Continued.
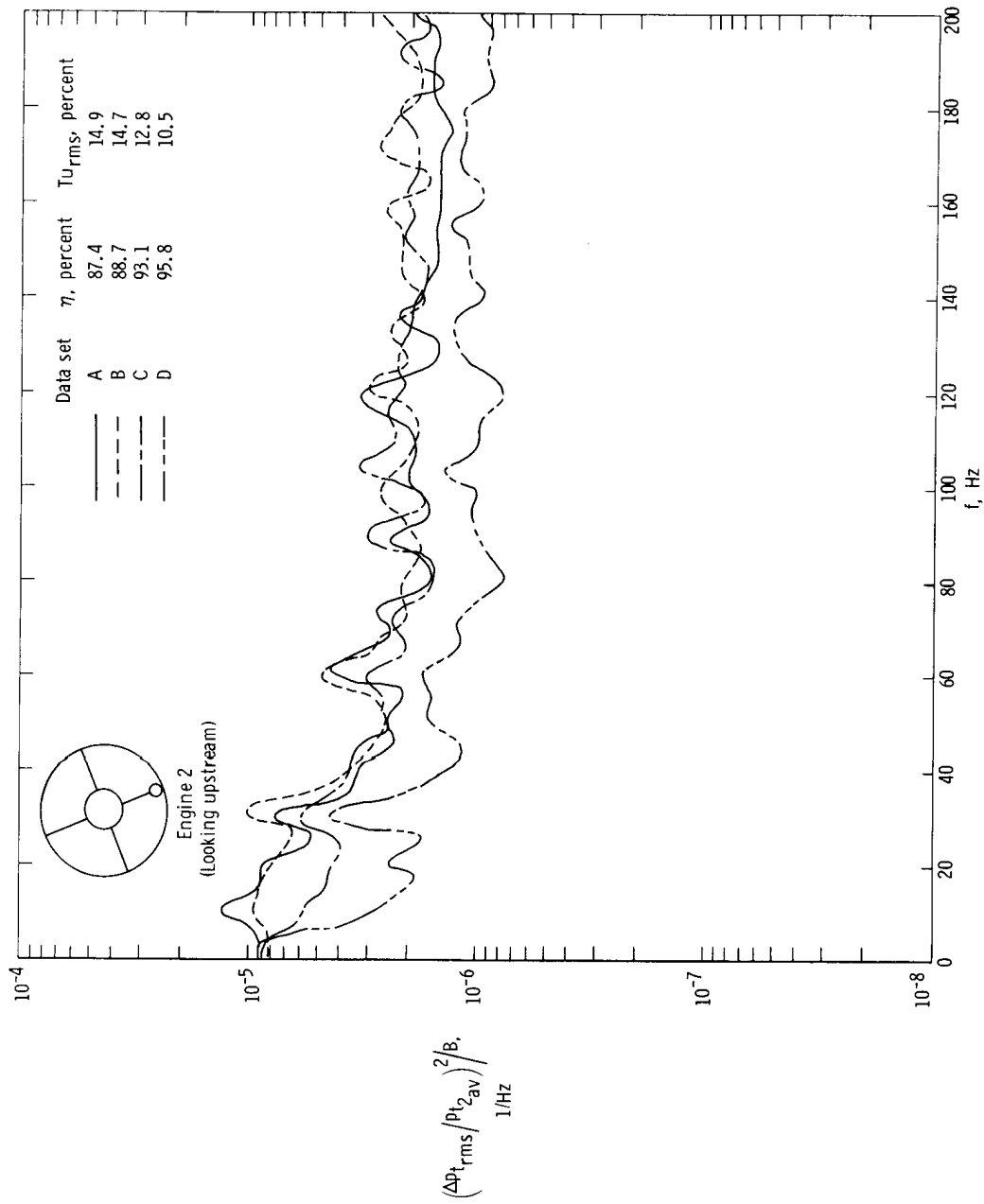
(h) Engine 2; rake 4; total-pressure probe 5.

Figure 14. – Continued.

42

(i) Engine 2; rake 6; total-pressure probe 1.

Figure 14. – Concluded.

(i) Engine 2; rake 6; total-pressure probe 1.

Figure 14. – Concluded.

Figure 15. – Inlet static-pressure and compressor-face total-pressure power spectral densities for M = 2.5 turbulence test conditions. n = 50; ϵ = 0.2; B = 5 Hz.

(a) Capped transducer (engine 2).

(b) Throat static-pressure sensor.

Figure 15.— Continued.

Data set	η, percent	Tu_{rms}, percent
E	82.3	5.7
F	74.4	7.1
G	68.2	9.5
H	65.7	10.3

(c) Duct static-pressure sensor.

Figure 15. – Continued.

(d) Engine 3; bullet-nose total-pressure probe.
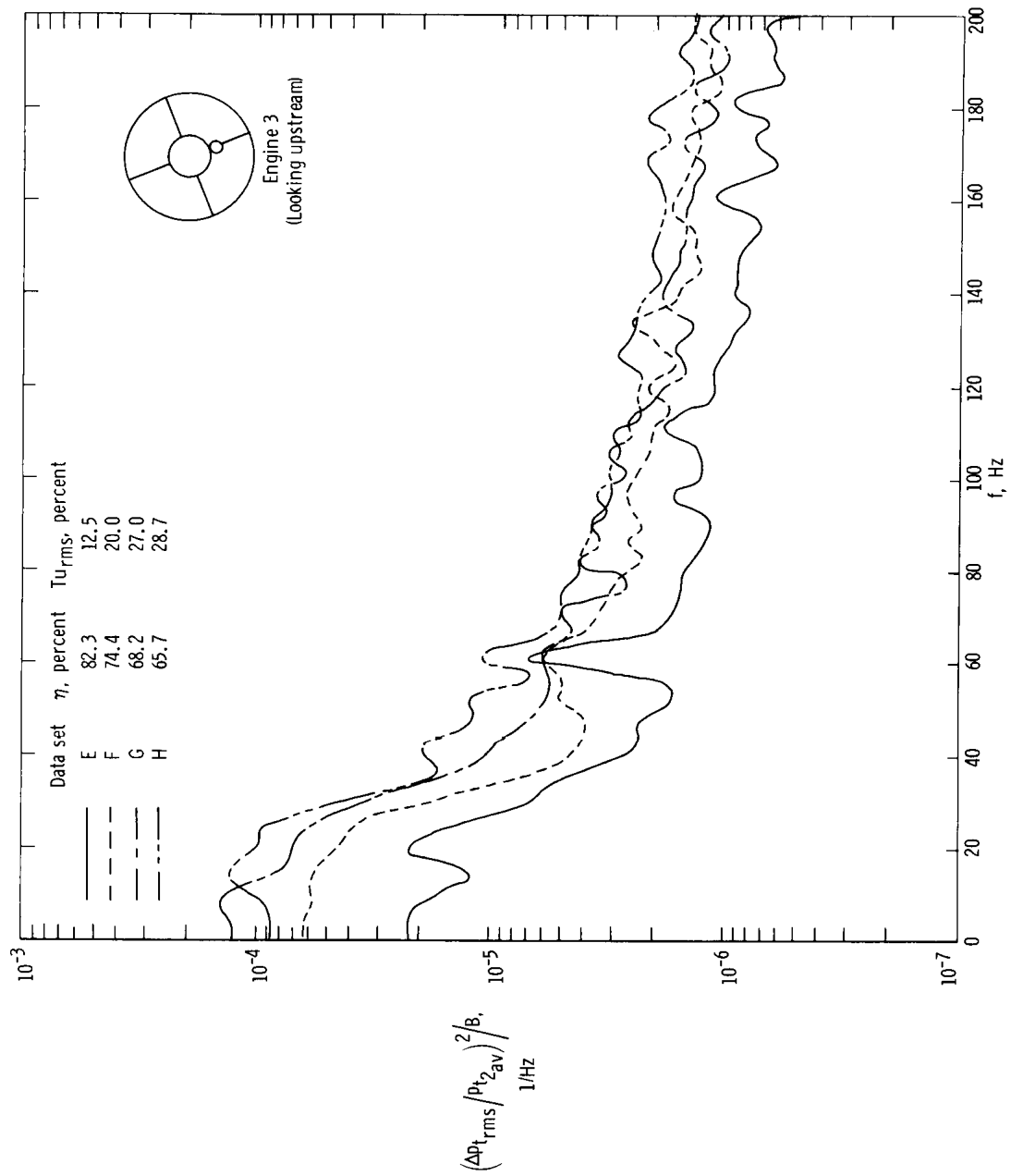
Figure 15. – Continued.

47

(e) Engine 3; rake 4; total-pressure probe 1.

Figure 15. – Continued.

48

(f) Engine 2; bullet-nose total-pressure probe.

Figure 15. — Continued.

(g) Engine 2; rake 4; total-pressure probe 1.

Figure 15. – Continued.

(h) Engine 2; rake 4; total-pressure probe 5.

Figure 15. – Continued.
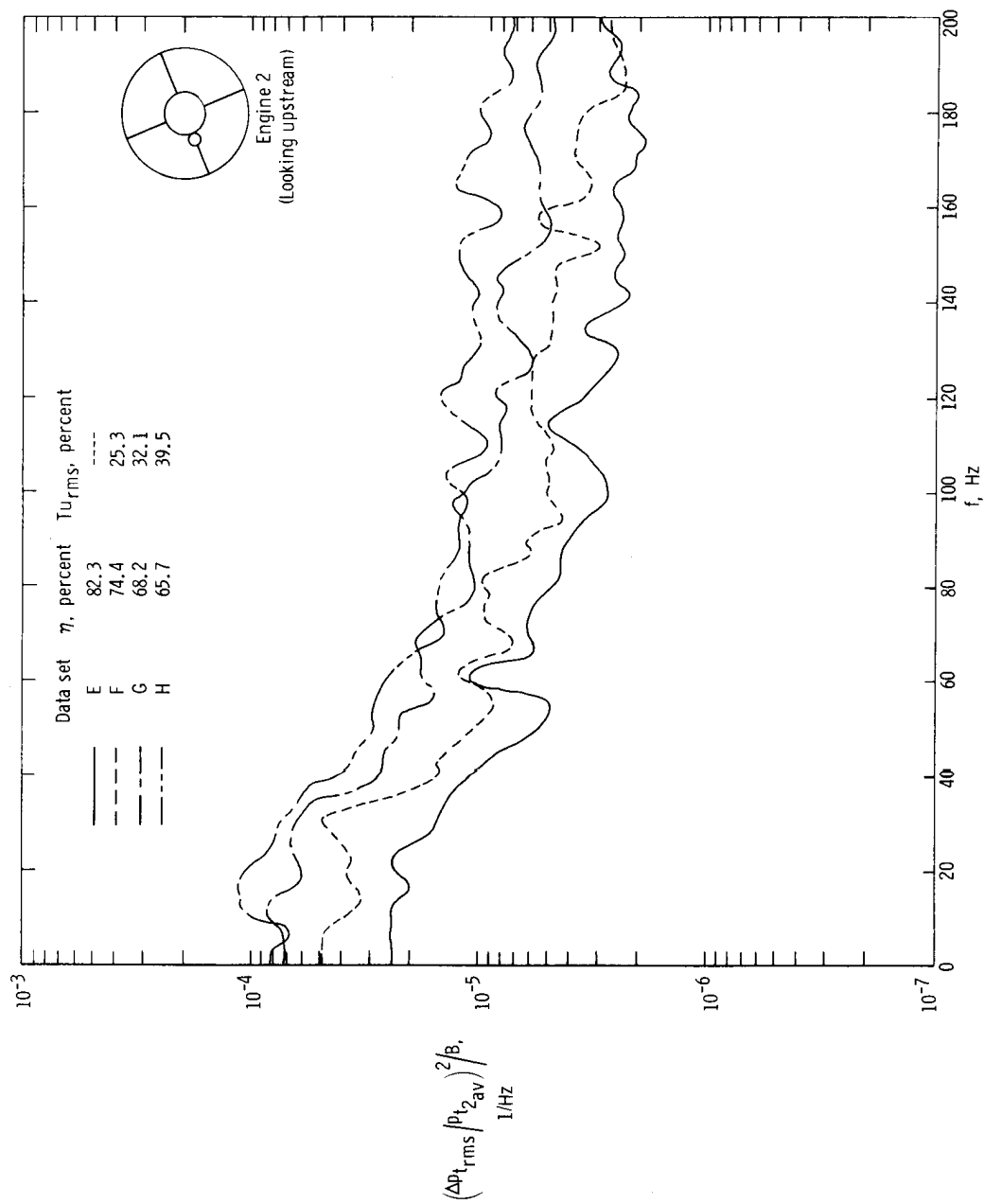
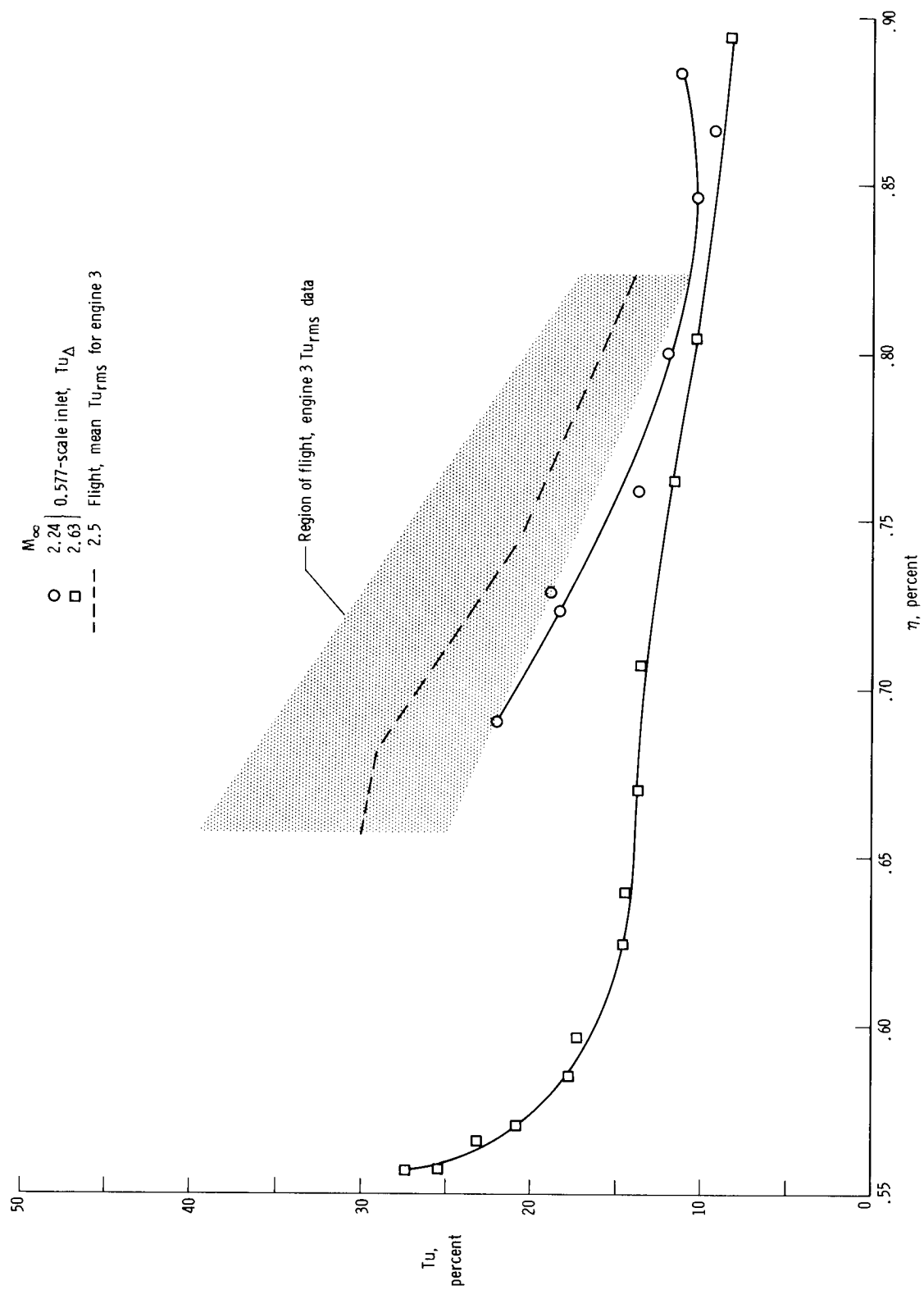(i) Engine 2; rake 6; total-pressure probe 1.

Figure 15. – Concluded.

Figure 16.— Comparison of flight and wind-tunnel turbulence variation with recovery.

□   Turbulence-generator instrumentation (high response)

O   XB-70-1 engine 2 instrumentation (high response)
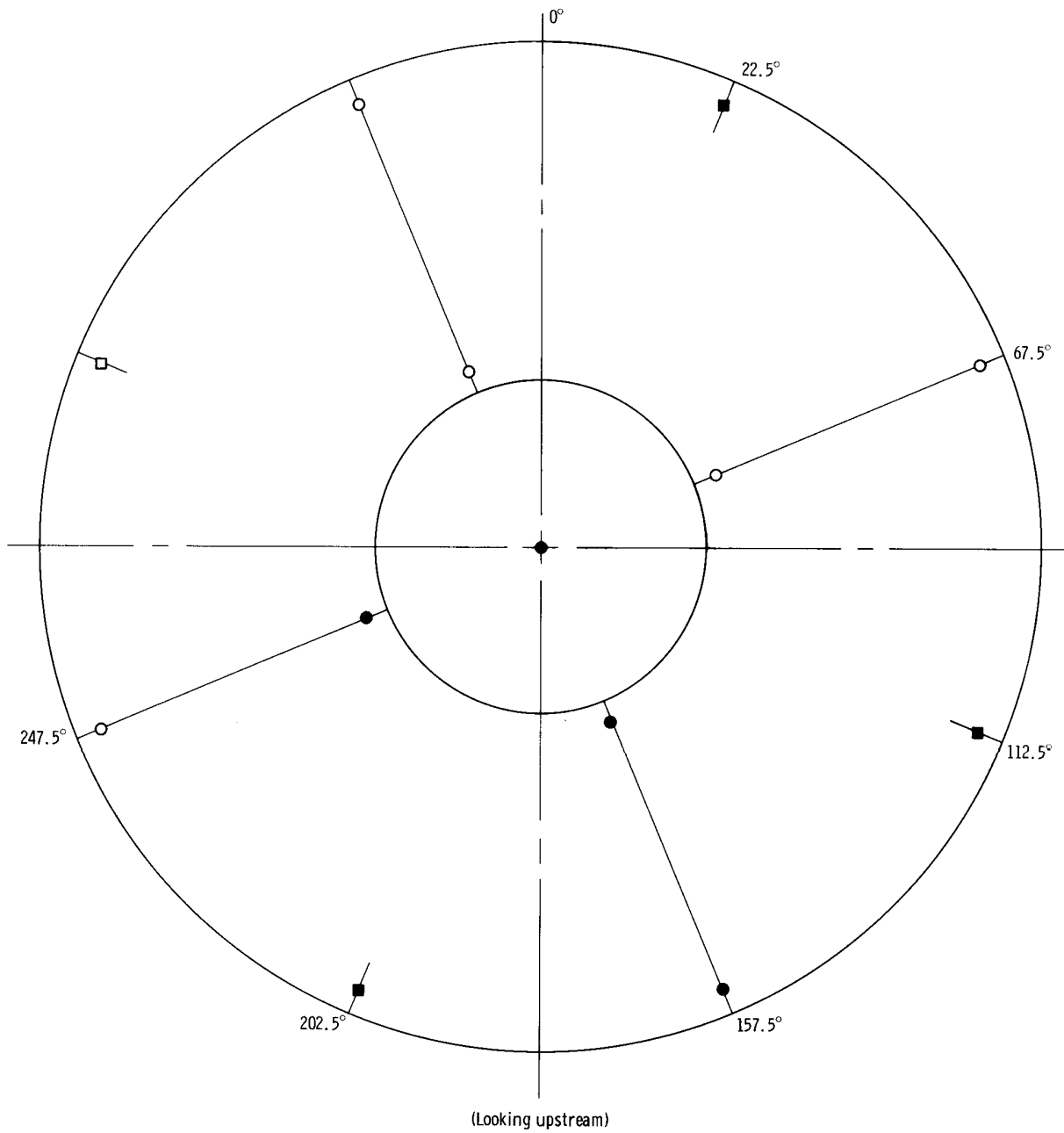Solid symbols denote probe locations for which data
are presented

(Looking upstream)

Figure 17.— Relative positions of engine 2 and turbulence-
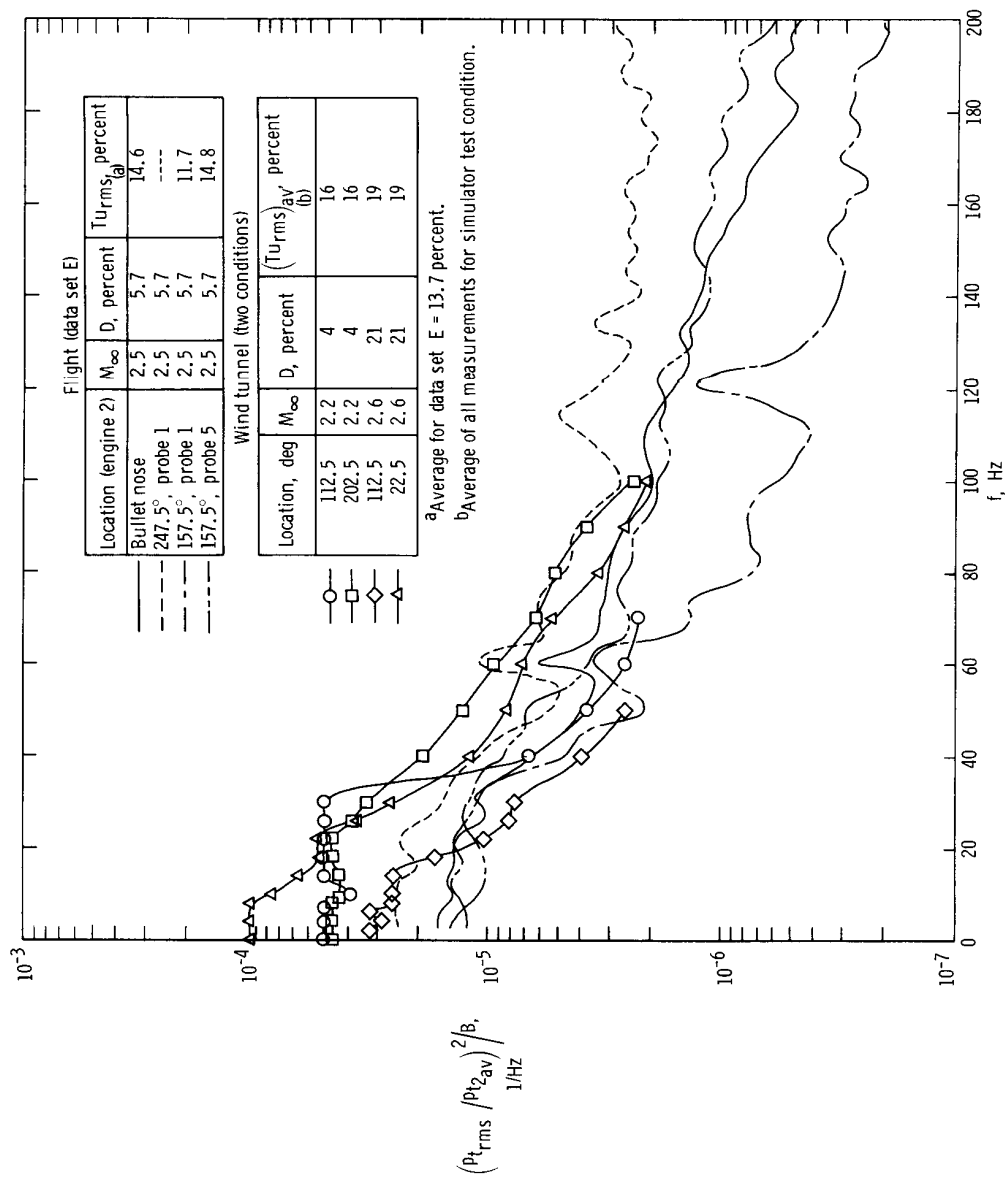generator high-response instrumentation.

54

Figure 18.— Comparison of flight and wind-tunnel compressor-face total-pressure power spectral density.
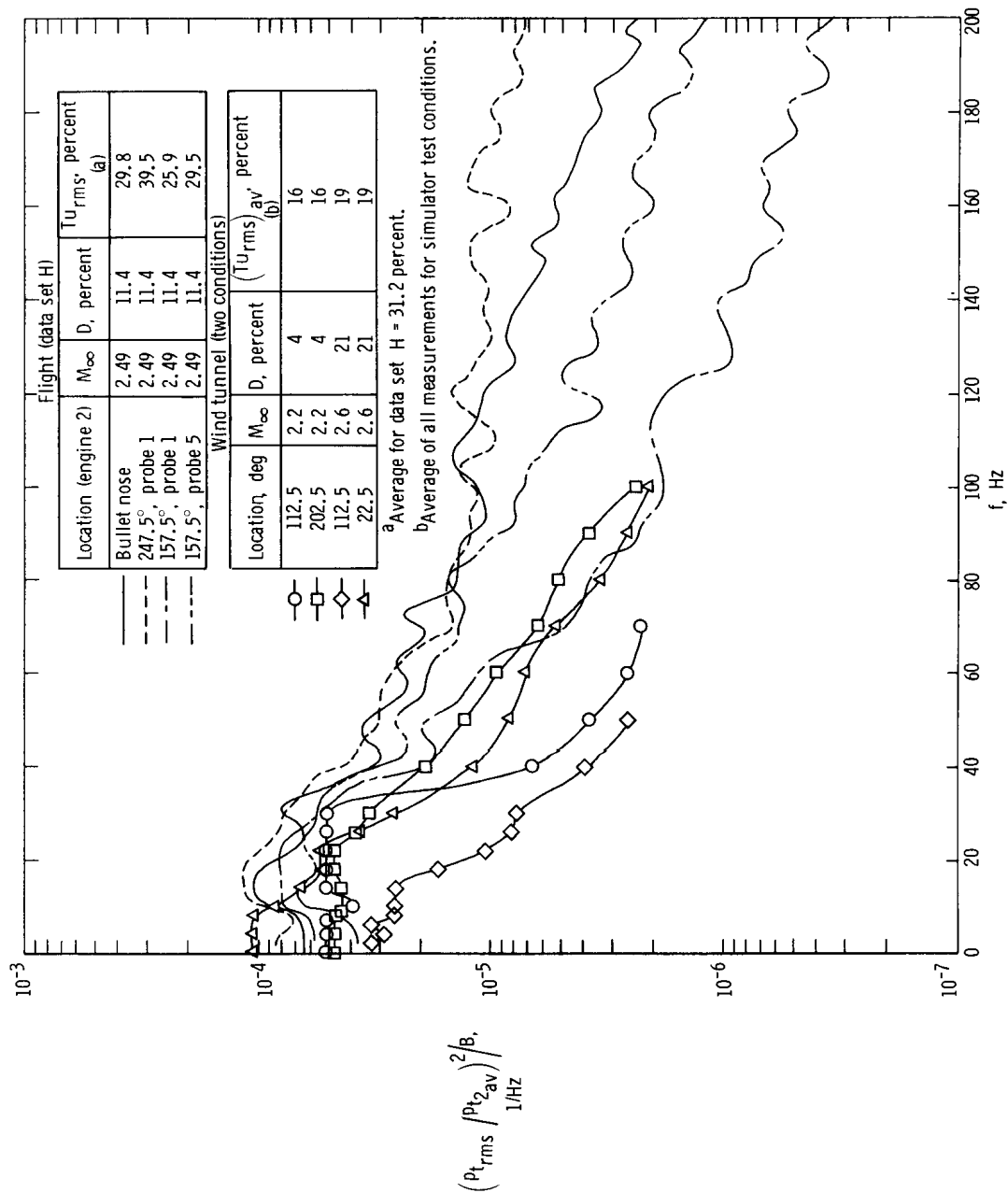
55

Figure 19.— Comparison of flight and wind-tunnel compressor-face total-pressure power spectral densities prior to stall.